A SPECTRAL VANISHING VISCOSITY METHOD FOR LARGE-EDDY SIMULATIONS OF TWO-FLUID FLOW

A THESIS SUBMITTED TO
THE GRADUATE SCHOOL OF ENGINEERING AND SCIENCE
OF BILKENT UNIVERSITY
IN PARTIAL FULFILLMENT OF THE REQUIREMENTS FOR
THE DEGREE OF
MASTER OF SCIENCE
IN
MECHANICAL ENGINEERING

By
Solmaz Khoshavaz
December 2020

A spectral vanishing viscosity method for large-eddy simulations of two-fluid flow
By Solmaz Khoshavaz
December 2020

We certify that we have read this thesis and that in our opinion it is fully adequate, in scope and in quality, as a thesis for the degree of Master of Science.

Luca Biancofiore(Advisor)

Metin Muradoğlu

Barbaros Çetin

Approved for the Graduate School of Engineering and Science:

Ezhan Karaşan
Director of the Graduate School

ABSTRACT

A SPECTRAL VANISHING VISCOSITY METHOD FOR LARGE-EDDY SIMULATIONS OF TWO-FLUID FLOW

Solmaz Khoshavaz
M.S. in Mechanical Engineering
Advisor: Luca Biancofiore
December 2020

DNS studies of turbulent flows have proved to be inefficient in terms of time and computational resources. On the other hand, Large-eddy simulation (LES) is an effective approach towards modeling turbulence. The current research applies an extension of the Spectral Vanishing Viscosity (SVV) method to finite differences. This straight-forward LES technique allows turbulence modeling without the need for filtering or upwinding. The result is a hybrid DNS/LES Solver.

The solver is applied to the two-fluid problem of falling liquid film in the presence of turbulent gas. Numerical simulation of falling liquid films requires a mathematical representation of the multiphase flow. A Direct Numerical Simulation (DNS) solver implementing finite volumes is used to solve the Navier-Stokes equations for the liquid phase. The Front Tracking method is used to model the moving gas-liquid interface.

Gravity-driven falling liquid films are commonplace in engineering applications. Perturbed falling films dramatically increase the heat/mass transport across the interface compared to flat films, which highlights the significance of studying interfacial flows. The present research aims to develop a numerical tool, which will be used to further investigate falling liquid film phenomena.

Keywords: turbulence, large-eddy simulation, spectral vanishing viscosity, two-fluid flow, falling liquid films.

ÖZET

İKİ SIVILI AKIŞLARDA GENİŞ GİRDAPLI SİMÜLASYONLAR IÇIN SPEKTRAL KAYBOLAN VISKOSITE YÖNTEMİ

Solmaz Khoshavaz
Makine Mühendisliği, Yüksek Lisans
Tez Danışmanı: Luca biancofiore
Aralık 2020

Türbülent akışlar için gerçekleştirilen DNS çalışmalarının, harcanan zaman ve sayısal kaynaklar açısından verimsizliği bilinmektedir. Öte yandan geniş girdap simülasyonları türbülent akışı modellemek açısından etkili bir yöntemdir. Mevcut araştırma Spectral Vanishing Viscosity (SVV) metodunun sonlu farklara uygulanmak üzere genişletilmesidir. LES tekniğinin kullanımı, filtreleme ve yukarı sarma metodunu uygulamadan türbülent akış modellemeyi mümkün kılmaktadır. Sonuç olarak hibrit bir DNS/LES solver oluşmaktadır.

Solver, türbülent akıştaki gaz eşliğinde yerçekimi etkisiyle akan sıvı bir film tabakasından oluşan iki akışkanlı bir probleme uygulanmıştır. Yerçekimi etkisiyle akan film tabakalarının numerik simülasyonları, çok fazlı akışların matematiksel gösterimlerine ihtiyaç duymaktadır. Sonlu hacimler üzerine uygulanan direkt numerik analiz ile sıvı faz için Navier-Stokes denklemleri çözdürülmüştür. Hareket halindeki sıvı-gaz arayüzünün modellenmesi için önizleme yöntemi kullanılmıştır.

Yerçekimi etkisinde akış gösteren sıvı filmler ile birçok endüstriyel uygulamada sıklıkla yer alır. Pertürbed düşen filmleri düz filmlere oranla ara yüzdeki ısı ve kütle transferini çarpıcı oranda arttırır. Bu durum ara yüzlü akışlara yönelik çalışmaların önemini arttırmaktadır. Mevcut çalışma ile geliştirilecek numerik aracın, ilerleyen zamanda düşen sıvı film olayının araştırılmasında kullanılması amaçlanmaktadır.

Anahtar sözcükler: türbülans, geniş girdaplı simülasyon, spektral kaybolan viskozite, düşen sıvı filmler .

Acknowledgement

I cannot begin to express my deepest gratitude to my supervisor, Dr. Luca Biancofiore, who continuously and patiently guided me through my master's research. The completion of my dissertation would not have been possible without his support and encouragement.

I would like to extend my sincere thanks to Prof. Metin Muradoğlu, who co-supervised a part of this research. I would also like to acknowledge the help of his student Ibrahim Nasuh Yildiran regarding the details of multiphase flow modeling and parallelization.

I would like to thank the examining committee members, Prof. Metin Muradoğlu, and Dr. Barbaros Çetin, for their insightful comments.

I very much appreciate my friends and colleagues at the FluidFrame Lab, particularly Hammam Mohamed for sharing his valuable experience and advice.

My sincere gratitude goes to my family and friends, especially to my best friend and life partner SEH, for their relentless love and moral support.

Finally, I thank Bilkent University, Mechanical Engineering Department for providing financial support throughout my master's studies.

Contents

List of Figures

List of Tables

Chapter 1

Introduction and Motivation

1.1 Motivation and Outline

Two-fluid flow is two immiscible fluids separated by an interface. A Commonplace example of two-fluid flow is liquid-gas interfaces. Numerical simulations of multiphase flow is a complicated and expensive task. In section 1.2 we discuss the available methodologies for multiphase flow modeling. Further in Chapter 2 a numerical model for multiphase flow is presented in 2.1. The model incorporates the Direct Numerical Simulations (DNS) of the Navier-Stokes equations (2.1.1) with Front tracking method (2.1.2) and Continuous Surface Force (CSF) method (2.1.3).

The DNS of turbulent flow is confirmed to be excessively time consuming and computationally expensive. Large Eddy Simulation (LES) of turbulent is a more efficient approach. Section 1.3 provides a brief introduction on numerical techniques in turbulence. Spectral Vanishing Viscosity (SVV) is the LES technique used in this work. The mathematical modeling of the SVV method is covered in section 2.2. A traditional implementation of the SVV method is discussed in 2.2.1. An extension of the SVV method from the spectral space to finite-differences is proposed in 2.2.2.

One of the widely encountered examples of two-fluid flow with interfacial turbulence is the problem of Falling Liquid Films. Falling Liquid Films are ubiquitous in both natural and engineering settings. In fact, falling liquid film phenomena play a critical role in industrial applications. Therefore, there has been a continuous and increasing curiosity about this topic among researchers. We select the problem of falling liquid films as a test case to investigate our numerical tool. Section 1.4 in this document is devoted to an introductory discussion on falling liquid films. The Surface Wave instability phenomena are described in 1.4.1. Chapter 3 includes the mathematical models corresponding to falling liquid films. This document does not aim to offer a comprehensive literature review on falling films. Accordingly, only the theory and mathematical models that are related to the goal of the research will be covered.

Finally, in Chapter 4 we present the validation of both multiphase flow DNS and LES solvers in 4.1 and 4.2 respectively. The final hybrid DNS/LES solver used to study the effect of turbulent co-current and counter-current gas in the case of laminar falling liquid films is presented in 4.3.

All in all, in this thesis, we develop a numerical tool to investigate the case-study of two-fluid flow with a liquid-gas interface. A numerical tool, written in FORTRAN Programming Language, is developed in which a front tracking method (2.1.2) is adopted to accurately predict the interface evolution, a Spectral Vanishing Viscosity (SVV) operator (2.2.2) is used to model smaller scales of turbulent structures in the gas phase, and Message Passing Interface (MPI) is implemented to parallelize the processes. The current numerical tool offers a novel platform for studying hydrodynamic instability and turbulence in falling liquid films as well as providing a foundation for investigating other phenomena in falling liquid films e.g. the Marangoni effect, evaporation, etc., which are further discussed in Chapter 5. Moreover, the hybrid solver can be used to study other two-fluid systems such as droplets in a turbulent flow.

1.2 Multiphase Flow

Two-fluid flows are two immiscible fluids separated by an interface (front). Multiphase flow constitutes a considerable part of the industry, for instance, heat transfer systems, process systems, and transport systems. Accurately predicting the behavior of multiphase flow is a problem of interest for both industrial and scientific research purposes. Numerical representation of multiphase flow and accounting for the topology of the interface is not trivial. In this research, we follow the methodology of Tryggvason [2] based on One-fluid approach. The one-fluid formulation is an approach for modeling two immiscible fluids separated by a sharp interface. In this approach, a single set of equations is applied to both phases and interface terms are added as singularity distributions. In this section, we introduce some of the most successful interface modeling techniques, which follow the one-fluid approach, including the Volume of Fluid (VOF) and the Front-tracking methods.

The VOF method (1981) is the oldest and widely used method to directly advect marker functions. In this method, the different fluids are directly identified. The fraction of the grid cell which is occupied by the fluid represents the marker function and is considered as the reference phase. The interface shape is approximately reconstructed using the volume fraction in each cell. The reconstructed interface is then advected in a given velocity field. The reference phase volumes are exchanged across the boundary of neighboring cells. The VOF method is incorporated in many open-source and commercial multiphase flow solvers.

The front tracking method (1992) introduced by Tryggvason and Unverdi [3] uses connected marker points to represent the sharp interface. The use of marker points yields superior results in terms of accuracy. In the front tracking method, we work with two grids: the fixed grid, on which the governing equations are solved and the lower dimensional grid that tracks the interface. The front grid makes the accurate advection of the interface possible.

One of the significant issues in the study of two-fluid flows is the stability and

the evolution of the interface between the fluids [4]. The front tracking method is capable of accurately modeling the interface topology compared to the VOF method. Furthermore, it produces a smooth transition of flow properties across the interface. Therefore, we choose the front tracking method as the interface modeling technique in this work. The numerical model associated with the front tracking method is elaborated in 2.1.2. This choice contributes to the novelty of the developed solver as the front tracking method is not implemented in other CFD software.

1.3 Turbulence

Turbulent flows are described as chaotic, irregular, unsteady, and random. The swirling motion of the fluid flow is referred to as eddy and it can occur on many scales. In this research, we are interested in developing a numerical tool to study a system of two-fluid flow in presence of turbulence. Numerically modeling multiphase flow is a complicated task, and accounting for turbulence adds to the complexity as well as computational expenses of the simulation. The Navier-Stokes equations describe all scales of the turbulent velocity field. However, an extensive amount of information is contained in the velocity field, which makes using the Direct Numerical Simulation (DNS) approach impractical.

Alternatively, Large Eddy Simulation (LES) is proved to be a more effective approach towards turbulence modeling [5]. LES of turbulent flow is a technique in which large scales of turbulent are explicitly resolved and the small scales are modeled. This is done by applying low-pass filtering to account for the large-scale structures. The residual part is known as subgrid-scale (SGS). Whereas, the DNS explicitly resolves all scales of the problem, thus, yielding undesirable computational time. Resolving the smaller scales using DNS is possible at the cost of decreasing the grid size, which is often not feasible due to limitations of computational power or data storage. Therefore, LES is advantageous thanks to the flexibility it offers to control the resolved scales, resulting in a more efficient solver. A comparison of DNS and LES is shown in figure 1.1.

The Spectral Vanishing Viscosity (SVV) is classified as an LES method. The SVV method was first proposed by E. Tadmor in 1989 [6] in the context of stabilizing Fourier spectral approximation of hyperbolic conservation laws. The SVV method of Tadmor introduces an artificial diffusion large enough to cutoff oscillations while maintaining the accuracy and the stability of the solution. The SVV operator is incorporated into the Navier-Stokes equations to control high wave number oscillations. The theory includes a vanishing viscosity amplitude defined in spectral space decreasing with the modenumber and a viscosity kernel for the high wavenumbers. The viscosity kernel acts as a switch function and is activated only in high wavenumbers [7]. A straightforward high-order numerical dissipation mimicking the SVV operator proposed by E. Lamballais *et al.* [8] is used in this research. The scheme has a spectral like accuracy, thus can resolve the details of the flow field. Moreover, the implementation of the turbulence model does not require any upwinding, which simplifies obtaining numerical stability.

As indicated in figure 1.2, the SVV method is rare in literature, which adds to the challenges of finding similar studies for validation purposes as well as contributing to extending the applications of this technique. In the current project, the SVV method is applied to simulate a liquid-gas problem in the scenario of falling liquid film. Our motivation for using the SVV technique emerges from the fact that it enables us to select the scales of the problem, which we want to resolve to a better degree compared to other LES models. Furthermore, it is appropriate for high-frequency wavenumbers, which are typical in turbulent interfacial flow. Moreover, the extension of the SVV method to finite differences provides a straight forward way of modeling small turbulent scales at a reasonable temporal and computational cost. The novelty of the present research lies in implementing an extension of the spectral SVV operator to the finite differences in the context of two-fluid flow modeled by a front-tracking method, as will be discussed in the following sections.

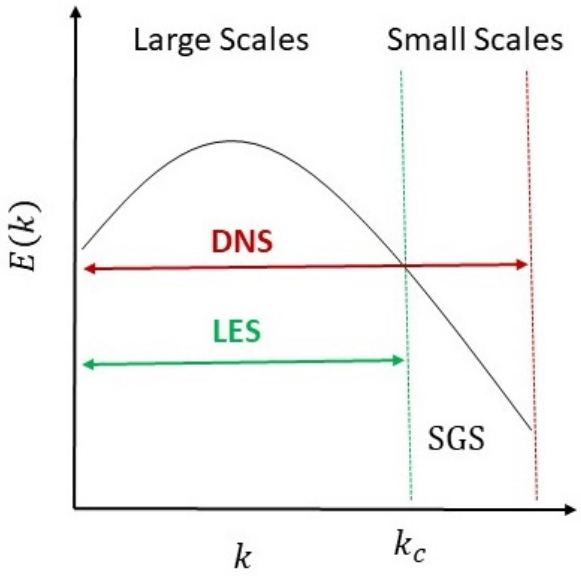

Figure 1.1: A comparison of DNS and LES in terms of energy versus wavenumber. DNS explicitly resolves for all the wavenumbers. Whereas, LES models wavenumbers that are higher than the cutoff wavenumber k_c.

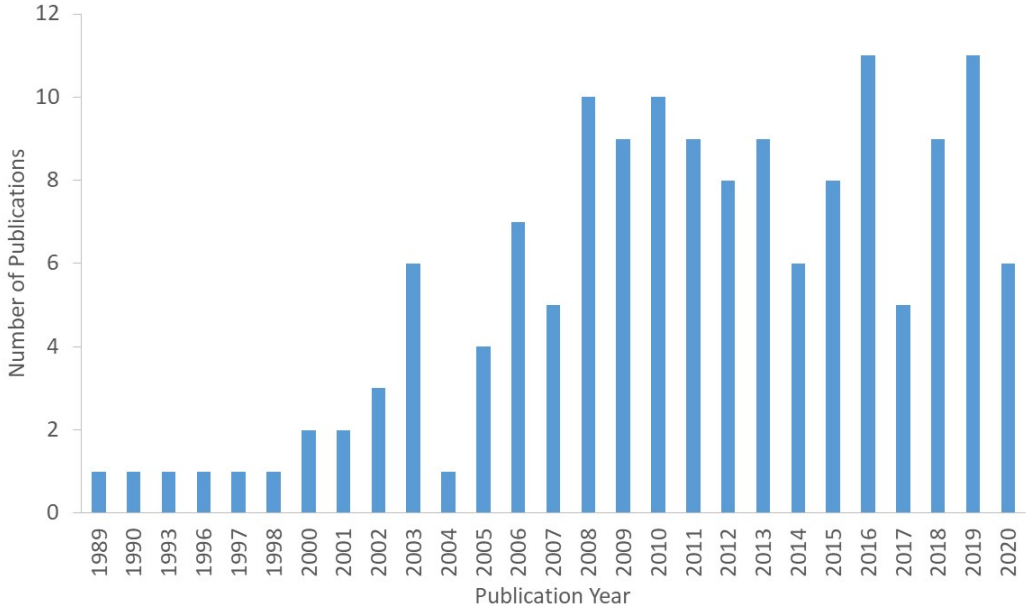

Figure 1.2: The number of publications on "Spectral Vanishing Viscosity" since 1989 with a total number of 147. Source: Web of Science, as of December 2020.

1.4 Falling Liquid Films

We take the test case of falling liquid films as an example of two-fluid flow in presence of turbulence. Falling liquid films are ubiquitous in both natural and engineering contexts. Wavy dynamics of falling liquid films can occur in very low Reynolds numbers [9]. Thus, they are easily observable on sloped sidewalks or on windows during rainy days as shown in figure 1.9. Falling Liquid Films in presence of turbulence are encountered in a wide range of technological and engineering applications, especially in chemical engineering processes. Typical examples of such applications include evaporators, condensers, cooling towers, heat exchangers, and distillation towers. Interfacial heat and mass transfer are shown to increase in the presence of waves [10]. Studies reveal that heat transfer can be 10-100% higher in a wavy film compared to a flat film [11,12]. In addition, the cooling mechanism of microelectronic equipment, and mass-heat transfer units in coating processes often use falling liquid films in presence of turbulent gas. The advanced techniques used in the food industry, e.g. separation process in the sugar industry, incorporate falling films [13].

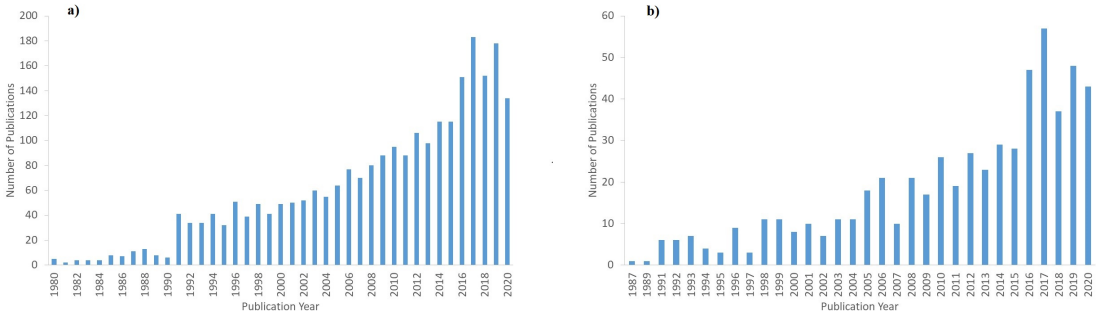

Figure 1.3: a) The number of publications on "Falling Liquid Films" since 1980 with a total number of 2494. b) The number of publications on numerical studies of Falling Liquid Films since 1980 with a total number of 580. Source: Web of Science, as of December 2020.

The Nobel Prize winner physicist, Leonidovitch Kapitza (1894-1984), was the first to conduct a well-controlled experiment on a falling film. He discovered a new form of wave motion in the concept of the thin film viscous liquid [13], including sinusoidal wave patterns with round peaks and troughs, and solitary waves of single drops. Such patterns show simple hydrodynamic instability driven by

inertia, which can result in spatio-temporal patterns of more complex instabilities [9]. Kapitza's pioneering work on both the experiment and the theory of falling liquid films established a foundation for further exploration of this topic. The advancements in the field of nonlinear dynamics and mathematical models (contributions of Benny, Shakadov, and Sivashinsky) [9] along with improved computational power culminated in a better understanding of falling liquid films. Following this path, there have been hundreds of documents in the form of research papers, books, and monographs devoted to this topic. Based on the data extracted from the Web of Science, as shown in figure 1.3, Falling Liquid Film has been continuously a topic of interest for researchers. Falling liquid films flowing in the presence of a counter-current gas flow are prevailing in engineering applications [5]. Several experimental works are dedicated to studying falling films sheared by a turbulent gas ([14–17]). Nonetheless, numerical studies of falling liquid films are few in number due to the complexity of modeling multiphase flow and accurately modeling the interface. The present research is devoted to developing a numerical platform that enables studying the evolution of the interface in falling liquid films with co-flowing and counter-flowing turbulent gas as well as providing a numerical platform to study instability and turbulence in the case of isothermal falling films.

1.4.1 Surface Wave Instability

In this section, we present the theory of surface wave instability in the example of falling liquid films. We will use this test case as a benchmark problem in section 4.1 to validate our multiphase DNS tool.

Experimental results of isothermal thin liquid films flowing down an inclined wall indicate the formation of "long" wavelength deformations on the free surface. In this context, "long" wavelength deformations imply deformations much longer than the film thickness, as depicted in figure 1.4. These long waves evolve from the instability of an initial uniform laminar flow profile (referred to as "flat film base flow"). This type of instability and its governing mechanisms are explained

in further detail as follows [13].

Surface wave instability also attributed as the Kapitza mode or H-mode is long-wave perturbations on the film surface influenced by three mechanisms [18]. Namely, the streamwise component of gravity, inertia, and the cross-stream component of gravity leading to hydrostatic pressure [13].

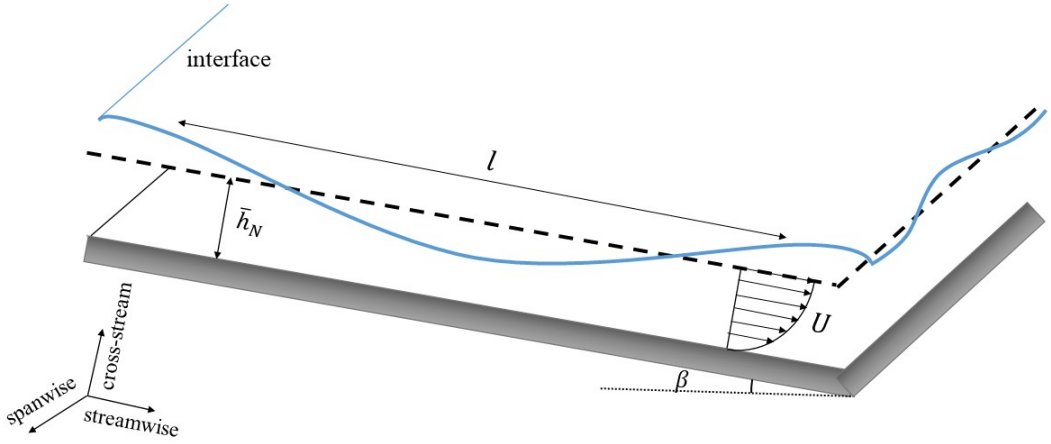

Figure 1.4: Schematic representation of a thin liquid film falling down an inclined plate of β degree. Mean film thickness is $\bar{h}_N$. The free surface is deflected over a length scale of l, which is much longer than the film thickness. The flow follows the semi-parabolic velocity profile of fully-developed viscous film flow shown as U. The figure is inspired by [13].

A long-wave perturbation is applied to the initially flat liquid film over a length scale of l as in figure 1.4. Consider the free surface is deflected upwards forming the crest of the wave. The height of the top surface gradually varies in the streamwise direction, therefore, each streamwise location closely follows the semi-parabolic velocity distribution of a fully developed viscous film flow. The net streamwise flow rate is positive and it increases with the depth of the film. Consequently, the maximum flow rate occurs at the crest of the perturbation and the minimum flow rate occurs at the trough. As a result, gravity draws the fluid at the front of the crest upwards while causing downward motion in the

back of the crest. Figure 1.5 shows a control volume over the front section of the crest, which experiences an inflow of Q_{in} and an outflow of $Q_{out} = 0$. The mass conservation implies the interface to move downwards. Likewise, the interface at the rear of the crest moves upward. The perturbation propagates as a result of these motions. This mechanism generates a wavy downstream motion of the perturbation without growth and at a phase speed higher than the velocity of any fluid particle in the initial undisturbed film [13].

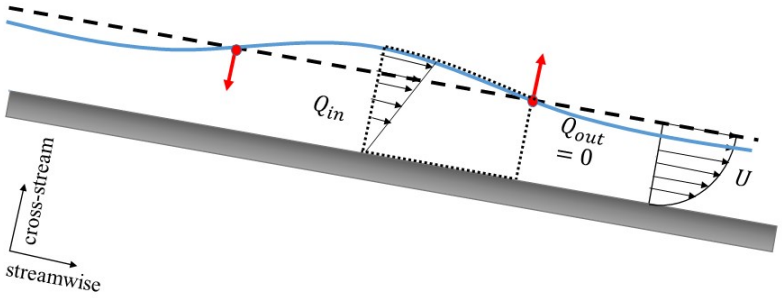

Figure 1.5: Upward/downward motion of the interface as a result of the streamwise component of gravity. The dashed line is the initial unperturbed free surface. The dotted box represents the control volume. A net flow Q_{in} enters the control volume. In order to satisfy the mass conservation, the interface must move upward. Similarly, the interface at the rear of the crest must move downward. Red arrows indicate the direction of the motion. The figure is inspired by [13].

Consider a streamwise location at a particular instance of time, as in figure 1.6. The surface height in front of the crest is increasing as a result of the forward propagation of the perturbation. Thus, the flow at this location tends to accelerate to follow the velocity profile of a fully developed viscous flow. However, the inertia prevents the flow from accelerating fast enough to fully follow the semi-parabolic velocity profile. As a result, the volume flux in the film is not as large as a film completely following the fully developed viscous profile. Similarly,

in the back of the crest, the surface height is decreasing and the flow tends to decelerate accordingly. The inertia prevents the flow from decelerating fast enough. Therefore, the volume flux at the rear is larger than the one expected from a flow following the fully developed viscous profile. The final result of these fluxes is the accumulation of fluid under the crest of the perturbation and an interfacial displacement as shown in figure 1.6 [13].

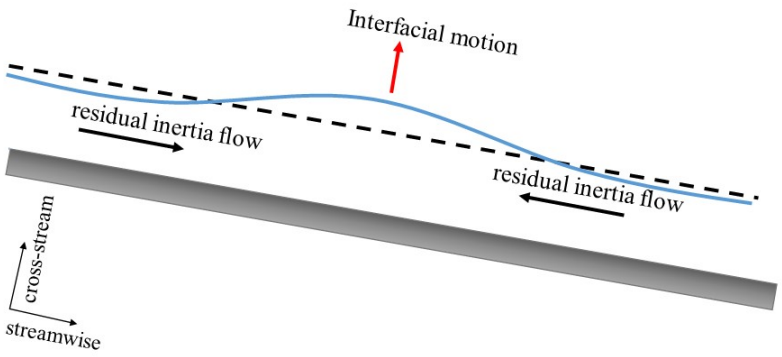

Figure 1.6: Interfacial motion as a result of the inertia effect. The black arrows show the residual inertia flow culminating in an increasing displacement in the crest of the wave (the red arrow). The figure is inspired by [13].

The cross-stream component of the gravity creates a hydrostatic pressure proportional to the film height, shown in figure 1.7. Under the crest, where the film has a higher depth, a positive pressure difference is imposed. Whereas, in the front and rear of the crest there is a negative change of hydrostatic pressure. As a result, the fluid tends to flow from the area with a larger dp to the area with a smaller dp, in the direction of the arrows shown in figure 1.7. This motion results in a downward motion of the crest, thus decreasing the amplitude of the perturbation and stabilizing the film. Nonetheless, the inertia effect opposes the effect of hydrostatic pressure. If the inertia dominates the hydrostatic pressure

the amplitude of the perturbation increases and the film becomes unstable (figure1.8). This mechanism sheds light on the unstable vertical falling films. Due to the absence of a cross-stream gravity component, there is no opposing mechanism to cancel the effect of inertia. Consequently, the film becomes unstable [13].

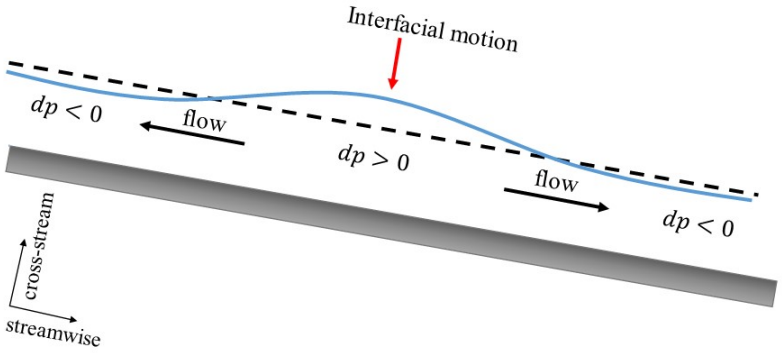

Figure 1.7: The cross-stream component of gravity generates a hydrostatic pressure proportional to the depth of the film. The flow moves from a region with larger pressure ($dp > 0$) towards a region with smaller pressure ($dp < 0$). Thus, the interface moves downward eventually resulting in a stable film. The figure is inspired by [13].

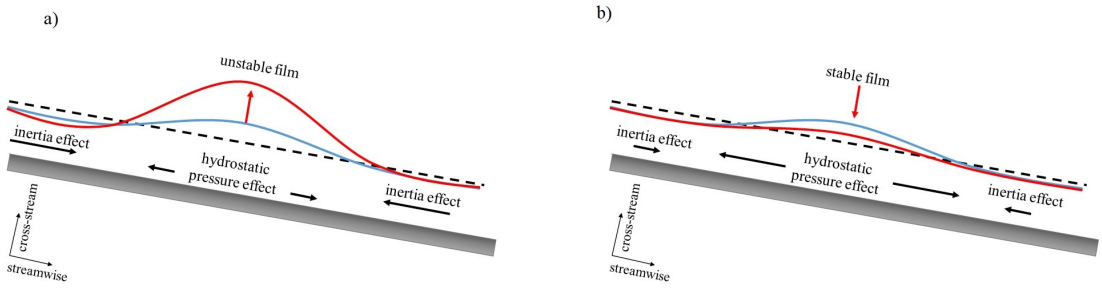

Figure 1.8: Role of inertia in hydrodynamic instability of surface waves. a) The inertia effect dominates the hydrostatic pressure effect. The fluid accumulates under the crest, which causes an increase in the perturbation leading to an unstable film. b) The hydrostatic pressure effect dominates the inertia effect, pushing the fluid towards the front and rear of the crest. As a result, the interface moves downwards. The perturbation amplitude decreases and the film eventually become stable.

Figure 1.9: A photograph of solitary wave formation in the case of rain falling down a slope. The photograph is taken by the author.

Chapter 2

Numerical Models

2.1 Multiphase Flow

Our two-fluid flow case of study incorporates two immiscible fluids: gas and liquid, and a free surface. Thanks to the advancements in modern computers and computational methods, precisely predicting the behavior of multiphase flows is feasible nowadays. The dynamics of multiphase flows are a topic of interest for both scientific and industrial intentions. This section emphasizes introducing the direct numerical simulations (DNS) of multiphase flows, implementing the front tracking method to capture the moving interface between the two phases. The method follows the "one-fluid" approach in which a single set of equations is used to model the flow field (including all phases). In this formulation, the interface is included as a singular distribution [2].

The equations governing the multiphase flow with interfaces are established based on the following general principles. The continuum assumption, which states the material can be treated as continuous regardless of the microscopic scales. Following the continuum hypothesis, we may make the assumption of sharp interfaces. The fluid properties such as density, viscosity, etc. follow a

gradual transition from one phase to another. Therefore, we can assume interfaces with vanishing thickness. Finally, we neglect the intermolecular forces. However, the role of such forces in interface physics is modeled by including surface tension [2].

The so-called one-fluid approach enables us to apply numerical methods developed for single-phase flows to solve for multiphase fields. Therefore, the governing equations stem from applying conservation of mass, conservation of momentum, and constitutive assumptions, which result in continuity and Navier-Stokes as in equations 3.1 and 3.2 respectively. We will elaborate on numerical solutions of these equations and their relation with interface modeling as follows.

2.1.1 Numerical Solutions of the Navier-Stokes Equations

We write the Navier-Stokes Momentum equation as:

$$\rho\frac{\partial \mathbf{v}}{\partial t} + \rho\mathbf{A} = -\nabla p + \mathbf{D} + \mathbf{f}, \tag{2.1}$$

where $\mathbf{v}(u, v, w)$ is the velocity vector with components in x,y,z directions respectively. $\mathbf{A} = \nabla.(\mathbf{vv})$ is the advection term and $\mathbf{D} = \nabla.\mu(\nabla\mathbf{v} + \nabla\mathbf{v}^T)$ is the diffusion term (also known as the viscous term). And $\mathbf{f}$ is the contribution of body force.

We start the discretizations by applying a first-order, explicit, forward marching in time. As a result, equation 2.1 can be written as:

$$\frac{\mathbf{v}^{n+1} - \mathbf{v}^n}{\Delta t} + \mathbf{A}_h^n = \frac{1}{\rho^n}(-\nabla_h p + \mathbf{D}_h^n + \mathbf{f}^n), \tag{2.2}$$

where Δt is the time step size. The superscript n indicates a value at the beginning of the time step and the superscript $n+1$ shows the value at the end of the time step. $\mathbf{A}_h$ and $\mathbf{D}_h$ are numerical approximations of advection and diffusion terms, respectively. ∇_h stands for the numerical approximation of gradient or

divergence operators. The continuity equation must be satisfied at the end of the time step. Thus, the velocity at the end of the time step must be divergent free:

$$\nabla_h.\mathbf{v}^{n+1} = 0. \tag{2.3}$$

Since there is no explicit term to account for the pressure in equations 2.2 and 2.3, we use the "Projection Method" to solve them. This method comprises two steps. First, the Predictor Step (2.4a), in which a temporary velocity field ($\mathbf{u}^*$) is found by neglecting the effect of the pressure terms in equation 2.2. Second, the Projection Step (2.4b), in which the pressure gradient is taken into account to find the velocity at the new time step.

$$\frac{\mathbf{v}^* - \mathbf{v}^n}{\Delta t} = -\mathbf{A}_h^n + \frac{1}{\rho^n}(\mathbf{D}_h^n + \mathbf{f}_h^n), \tag{2.4a}$$

$$\frac{\mathbf{v}^{n+1} - \mathbf{v}^*}{\Delta t} = \frac{1}{\rho^n}(-\nabla_h p). \tag{2.4b}$$

Equations 2.4a and 2.4b add up to be equal to equation 2.2 as the temporary velocity field cancels out in the summation.

As mentioned earlier, the continuity equation is satisfied when the velocity at the end of the time step is divergent free. Therefore, we want to find the pressure such that it yields divergent free velocity. In order to apply this condition, we take the divergent of equation 2.4b and we plug in equation 2.3:

$$\nabla_h.(\frac{1}{\rho^n}\nabla_h p) = \frac{1}{\Delta t}\nabla_h.\mathbf{v}^*. \tag{2.5}$$

This is the Poisson equation for the pressure. The resolved pressure field and the temporary velocity field will then be used to correct the velocity, resulting in the velocity at the new time step:

$$\mathbf{u}^{n+1} = \mathbf{u}^* - \frac{\Delta t}{\rho^n} \nabla_h p. \tag{2.6}$$

Notice that to ensure numerical stability for the introduced explicit scheme, the time step must be small enough. The advection and the diffusion terms restrict the value of Δt. The discretization scheme of the diffusion terms is second-order, central differencing approximation which requires:

$$\frac{\mu \Delta t}{\rho h^2} \leq \frac{1}{4} \text{ for 2D}, \tag{2.7a}$$

$$\frac{\mu \Delta t}{\rho h^2} \leq \frac{1}{6} \text{ for 3D}, \tag{2.7b}$$

where h is the smallest grid spacing. Criterions (2.7a) and (2.7b) are used in two-dimensions and three-dimensions respectively.

Stability criterion for a second-order central differencing approximation of the advection terms requires:

$$(\mathbf{v} \cdot \mathbf{v}) \frac{\rho \Delta t}{\mu} \leq 2. \tag{2.8}$$

Moreover, the stability of temporal and spatial discretizations depend on the Courant-Friedrich Lewy (CFL) condition as:

$$\frac{|\mathbf{v}_{max}| \Delta t}{h} \leq 1, \tag{2.9}$$

where $|\mathbf{v}_{max}|$ is the magnitude of maximum velocity. This condition guarantees that Δt is adequately small so that a material point travels less than one grid spacing in each time step.

We use the finite-volume method for spatial discretizations. Before proceeding to the discretization of advection and diffusion terms, we discuss the selected

control volume and mesh. We use the staggered grid in which discrete variables such as velocity, pressure, and fluid properties are stored at a separate grid as shown in figure 2.1. Using the staggered mesh makes the derivation of boundary conditions straightforward. Assume a control volume around the pressure nodes (outlined by the blue line). As imposed by the continuity principle for incompressible flows, the pressure must enforce a divergence free velocity field. Therefore, a net inflow into this control volume leads to a rise in pressure, a net outflow results in a decrease of pressure. The horizontal velocity components (u) and the vertical velocity components (v) are located at the middle boundaries of the control volume. Consequently, the grid for the horizontal velocity is shifted half a grid cell to the right from the pressure node, and the grid for the vertical velocity is shifted half a grid cell upward. Likewise, the third component of velocity (w) can be located on the staggered grid; however, we sketch a two-dimensional grid for simplicity and to avoid confusion. The three-dimensional representation of one cell is given in figure 2.2 in order to simplify the following derivations in the third dimension. Furthermore, the location of the pressure nodes and the velocity nodes is shown for a two-dimensional computational domain of 4×4. The crosshatched area includes the ghost nodes, which will be used in the definition of boundary conditions in the later steps.

To discretize the momentum equation we use a finite volume scheme. Using the divergence theorem, the average value of advection term and diffusion term over a control volume are:

$$\mathbf{A}_c = \frac{1}{V}\int_V \nabla \cdot (\mathbf{vv}) dv = \frac{1}{V}\oint_S \mathbf{v}(\mathbf{v}.\mathbf{n}) ds, \tag{2.10}$$

$$\mathbf{D}_c = \frac{1}{V}\int_V \nabla \cdot \mathbf{T}^v dv = \frac{1}{V}\oint_S \mathbf{n}.\mathbf{T}^v ds, \tag{2.11}$$

where $V = \Delta x \times \Delta y \times \Delta z$ is the volume of the three-dimensional rectangular control volume, and $\mathbf{T}^v$ is the viscous stress tensor for incompressible flow:

$$\mathbf{T}^v = \mu[\nabla_h \mathbf{v} + (\nabla_h \mathbf{v})^T]. \tag{2.12}$$

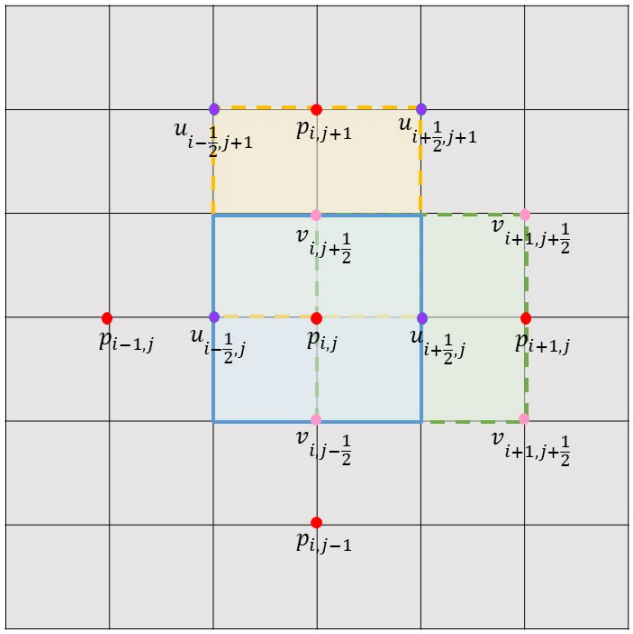

Figure 2.1: The pressure nodes (red points) are located at the center of the control volume (outlined by blue). The control volume for the horizontal velocity (purple points) is located at half a mesh to the right of the pressure node (outlined by green). The control volume for the vertical velocity (pink points) is located at half a mesh upward to the pressure node (outlined by yellow).

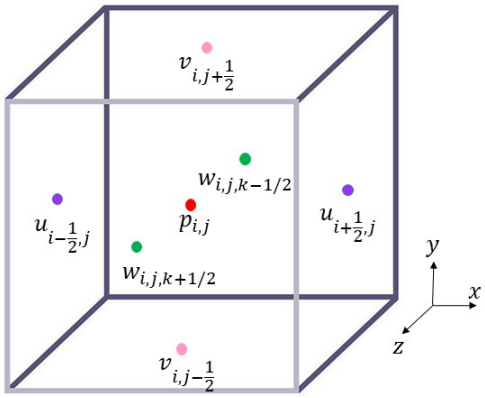

Figure 2.2: The pressure node (the red point) is located at the center of the control volume. The velocity component nodes of u,v,w are shown by purple, pink, and green points respectively.

The average value of the pressure gradient is:

$$(\nabla p)_c = \frac{1}{V}\int_V \nabla p dv = \frac{1}{V}\oint_S p\mathbf{n}ds. \tag{2.13}$$

The average value of body force is:

$$\mathbf{f}_c = \frac{1}{V}\int_V f(x)dv. \tag{2.14}$$

The integral form of continuity equation at time step $n+1$ is:

$$\oint_S \mathbf{v}^{n+1}.\mathbf{n}ds = 0. \tag{2.15}$$

Discretizing equation 2.3 on the staggered grid shown in figure 2.1 the continuity equation on the control volume becomes:

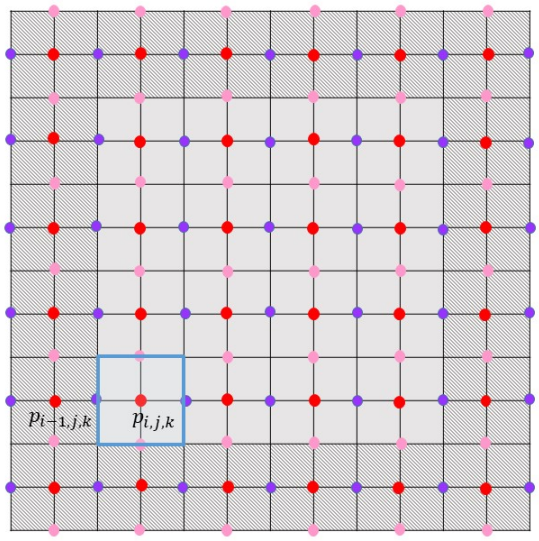

Figure 2.3: The plot of a two-dimensional 4×4 staggered grid. The pressure nodes (red points) are located at the center of the control volume (outlined by blue). The velocity component nodes of u, and v are shown by purple, and pink points respectively. The crosshatched region embodies the ghost nodes, which are used in defining the boundary conditions.

$$\frac{u^{n+1}_{i+1/2,j,k} - u^{n+1}_{i-1/2,j,k}}{\Delta x} + \frac{v^{n+1}_{i,j+1/2,k} - v^{n+1}_{i,j-1/2,k}}{\Delta y} + \frac{w^{n+1}_{i,j,k+1/2} - w^{n+1}_{i,j,k-1/2}}{\Delta z} = 0. \quad (2.16)$$

The discretized form of equation (2.4a) is given below and it results in temporary velocity field components:

$$u^*_{i+1/2,j,k} = u^n_{i+1/2,j,k} + \Delta t[-(A_x)^n_{i+1/2,j,k} + (g_x)^n_{i+1/2,j,k} + \frac{1}{1/2(\rho^n_{i,j,k} + \rho^n_{i+1,j,k})}(D_x)^n_{i+1/2,j,k}], \quad (2.17)$$

$$v^*_{i,j+1/2,k} = v^n_{i,j+1/2,k} + \Delta t[-(A_y)^n_{i,j+1/2,k} + (g_y)^n_{i,j+1/2,k} + \frac{1}{1/2(\rho^n_{i,j,k} + \rho^n_{i,j+1,k})}(D_y)^n_{i,j+1/2,k}], \quad (2.18)$$

$$w^*_{i,j,k+1/2} = w^n_{i,j,k+1/2} + \Delta t[-(A_z)^n_{i,j,k+1/2} + (g_z)^n_{i,j,k+1/2} + \frac{1}{1/2(\rho^n_{i,j,k} + \rho^n_{i,j,k+1})}(D_z)^n_{i,j,k+1/2}], \quad (2.19)$$

where A_x, A_y and A_z are numerical approximations of the advection term in equation (2.10). And D_x, D_y and D_z are numerical approximations of the diffusion term in equation(2.11).

Using the same staggered grid, we discretize equation (2.4b):

$$u^n_{i+1/2,j,k} = u^*_{i+1/2,j,k} - \frac{\Delta t}{1/2(\rho^n_{i,j,k} + \rho^n_{i+1,j,k})}\frac{p^n_{i+1,j,k} - p^n_{i,j,k}}{\Delta x}, \quad (2.20a)$$

$$v^n_{i,j+1/2,k} = v^*_{i,j+1/2,k} - \frac{\Delta t}{1/2(\rho^n_{i,j,k} + \rho^n_{i,j+1,k})}\frac{p^n_{i,j+1,k} - p^n_{i,j,k}}{\Delta y}, \quad (2.20b)$$

$$w^n_{i,j,k+1/2} = w^*_{i,j,k+1/2} - \frac{\Delta t}{1/2(\rho^n_{i,j,k} + \rho^n_{i,j,k+1})}\frac{p^n_{i,j,k+1} - p^n_{i,j,k}}{\Delta z}. \quad (2.20c)$$

Similarly, we can write equation (2.4b) for the other side of the control volume:

$$u^n_{i-1/2,j,k} = u^*_{i-1/2,j,k} - \frac{\Delta t}{1/2(\rho^n_{i-1,j,k} + \rho^n_{i,j,k})} \frac{p^n_{i,j,k} - p^n_{i-1,j,k}}{\Delta x}, \tag{2.21a}$$

$$v^n_{i,j-1/2,k} = v^*_{i,j-1/2,k} - \frac{\Delta t}{1/2(\rho^n_{i,j-1,k} + \rho^n_{i,j,k})} \frac{p^n_{i,j,k} - p^n_{i,j-1,k}}{\Delta y}, \tag{2.21b}$$

$$w^n_{i,j,k-1/2} = w^*_{i,j,k-1/2} - \frac{\Delta t}{1/2(\rho^n_{i,j,k-1} + \rho^n_{i,j,k})} \frac{p^n_{i,j,k} - p^n_{i,j,k-1}}{\Delta z}. \tag{2.21c}$$

Substituting equations (2.20) and (2.21) in equation (2.16) results in the pressure equation:

$$\begin{aligned} &\frac{1}{\Delta x^2}\left(\frac{p_{i+1,j,k} - p_{i,j,k}}{\rho^n_{i+1,j,k} + \rho^n_{i,j,k}} - \frac{p_{i,j,k} - p_{i-1,j,k}}{\rho^n_{i,j,k} + \rho^n_{i-1,j,k}}\right) + \\ &\frac{1}{\Delta y^2}\left(\frac{p_{i,j+1,k} - p_{i,j,k}}{\rho^n_{i,j+1,k} + \rho^n_{i,j,k}} - \frac{p_{i,j,k} - p_{i,j-1,k}}{\rho^n_{i,j,k} + \rho^n_{i,j-1,k}}\right) + \\ &\frac{1}{\Delta z^2}\left(\frac{p_{i,j,k+1} - p_{i,j,k}}{\rho^n_{i,j,k+1} + \rho^n_{i,j,k}} - \frac{p_{i,j,k} - p_{i,j,k-1}}{\rho^n_{i,j,k} + \rho^n_{i,j,k-1}}\right) = \\ &\frac{1}{2\Delta t}\left(\frac{u^*_{i+1/2,j,k} - u^*_{i-1/2,j,k}}{\Delta x} + \frac{v^*_{i,j+1/2,k} - v^*_{i,j-1/2,k}}{\Delta y} + \frac{w^*_{i,j,k+1/2} - w^*_{i,j,k-1/2}}{\Delta z}\right). \end{aligned} \tag{2.22}$$

This is the Poisson equation for pressure. There are several methods to solve the pressure equation (2.22). One of the most convenient solvers is a simple successive over-relaxation (SOR) iteration method. The pressure equation must be rearranged such that the $p_{i,j,k}$ term is isolated on the left-hand side:

$$
\begin{aligned}
p_{i,j,k}[&\frac{2\Delta t}{\Delta x^2(\rho^n_{i+1,j,k}+\rho^n_{i,j,k})}+\frac{2\Delta t}{\Delta x^2(\rho^n_{i,j,k}+\rho^n_{i-1,j,k})}+\\
&\frac{2\Delta t}{\Delta y^2(\rho^n_{i,j+1,k}+\rho^n_{i,j,k})}+\frac{2\Delta t}{\Delta y^2(\rho^n_{i,j,k}+\rho^n_{i,j-1,k})}+\\
&\frac{2\Delta t}{\Delta z^2(\rho^n_{i,j,k+1}+\rho^n_{i,j,k})}+\frac{2\Delta t}{\Delta z^2(\rho^n_{i,j,k}+\rho^n_{i,j,k-1})}]=\\
p_{i-1,j,k}[&\frac{2\Delta t}{\Delta x^2(\rho^n_{i-1,j,k}+\rho^n_{i,j,k})}]+p_{i+1,j,k}[\frac{2\Delta t}{\Delta x^2(\rho^n_{i+1,j,k}+\rho^n_{i,j,k})}]+\\
p_{i,j-1,k}[&\frac{2\Delta t}{\Delta y^2(\rho^n_{i,j-1,k}+\rho^n_{i,j,k})}]+p_{i,j+1,k}[\frac{2\Delta t}{\Delta y^2(\rho^n_{i,j+1,k}+\rho^n_{i,j,k})}]+\\
p_{i,j,k-1}[&\frac{2\Delta t}{\Delta z^2(\rho^n_{i,j,k-1}+\rho^n_{i,j,k})}]+p_{i,j,k+1}[\frac{2\Delta t}{\Delta z^2(\rho^n_{i,j,k+1}+\rho^n_{i,j,k})}]-\\
[&\frac{u^*_{i+1/2,j,k}-u^*_{i-1/2,j,k}}{\Delta x}+\frac{v^*_{i,j+1/2,k}-v^*_{i,j-1/2,k}}{\Delta y}+\frac{w^*_{i,j,k+1/2}-w^*_{i,j,k-1/2}}{\Delta z}].
\end{aligned}
\tag{2.23}
$$

Then, the SOR iterative method resolves the pressure:

$$
\begin{aligned}
p^{\alpha+1}_{i,j,k}=\beta[&\frac{1}{\Delta x^2}(\frac{1}{\rho^n_{i+1,j,k}+\rho^n_{i,j,k}}-\frac{1}{\rho^n_{i,j,k}+\rho^n_{i-1,j,k}})+\\
&\frac{1}{\Delta y^2}(\frac{1}{\rho^n_{i,j+1,k}+\rho^n_{i,j,k}}-\frac{1}{\rho^n_{i,j,k}+\rho^n_{i,j-1,k}})+\\
&\frac{1}{\Delta z^2}(\frac{1}{\rho^n_{i,j,k+1}+\rho^n_{i,j,k}}-\frac{1}{\rho^n_{i,j,k}+\rho^n_{i,j,k-1}})+\\
\frac{1}{2\Delta t}(&\frac{u^*_{i+1/2,j,k}-u^*_{i-1/2,j,k}}{\Delta x}+\frac{v^*_{i,j+1/2,k}-v^*_{i,j-1/2,k}}{\Delta y}+\frac{w^*_{i,j,k+1/2}-w^*_{i,j,k-1/2}}{\Delta z})]+(1-\beta)p^{\alpha}_{i,j,k},
\end{aligned}
\tag{2.24}
$$

where $p^{\alpha}_{i,j,k}$ is the pressure from the last iteration α and $p^{\alpha+1}_{i,j,k}$ is the new approximation of the pressure. The relaxation parameter β must be $\beta > 1$ for over relaxation. The stability of the method requires $\beta < 2$. A value of $\beta = 1.2$–1.5 is an appropriate choice for the relaxation parameter.

While the SOR method is an effective way of resolving the pressure field, it may be excessively time-consuming depending on the dimensions of the problem and the desired accuracy. A faster alternative approach is using multigrid methods offered by open-source mathematical libraries such as HYPRE. The PFMG solver of HYPRE is used in this research to solve the Poisson equation.

The average value of advection and diffusion terms (equations (2.10) and (2.11)) can be approximated using the midpoint rule. We start from equation (2.11) to approximate the integral of viscous fluxes:

$$(D_x)^n_{i+1/2,j,k} = \frac{T^{v,xx}_{i+1,j,k} - T^{v,xx}_{i,j,k}}{\Delta x} + \frac{T^{v,xy}_{i+1/2,j+1/2,k} - T^{v,xy}_{i+1/2,j-1/2,k}}{\Delta y} + \frac{T^{v,xz}_{i+1/2,j,k+1/2} - T^{v,xz}_{i+1/2,j,k-1/2}}{\Delta z}, \tag{2.25a}$$

$$(D_y)^n_{i,j+1/2,k} = \frac{T^{v,yx}_{i+1/2,j+1/2,k} - T^{v,yx}_{i-1/2,j+1/2,k}}{\Delta x} + \frac{T^{v,yy}_{i,j+1,k} - T^{v,yy}_{i,j,k}}{\Delta y} + \frac{T^{v,yz}_{i,j+1/2,k+1/2} - T^{v,yz}_{i,j+1/2,k-1/2}}{\Delta z}, \tag{2.25b}$$

$$(D_z)^n_{i,j,k+1/2} = \frac{T^{v,zx}_{i+1/2,j,k+1/2} - T^{v,zx}_{i-1/2,j,k+1/2}}{\Delta x} + \frac{T^{v,zy}_{i,j+1/2,k+1/2} - T^{v,zy}_{i,j-1/2,k+1/2}}{\Delta y} + \frac{T^{v,zz}_{i,j,k+1} - T^{v,zz}_{i,j,k}}{\Delta z}. \tag{2.25c}$$

The viscous stress tension terms $\mathbf{T}^v$ are approximated using standard second-order central differencing:

$$T^{v,xx}_{i,j,k} = 2\mu^n_{i,j,k}\frac{u^n_{i+1/2,j,k} - u^n_{i-1/2,j,k}}{\Delta x}, \tag{2.26a}$$

$$T^{v,yy}_{i,j,k} = 2\mu^n_{i,j,k}\frac{v^n_{i,j+1/2,k} - v^n_{i,j-1/2,k}}{\Delta y}, \tag{2.26b}$$

$$T^{v,zz}_{i,j,k} = 2\mu^n_{i,j,k}\frac{w^n_{i,j,k+1/2} - w^n_{i,j,k-1/2}}{\Delta z}, \tag{2.26c}$$

$$T^{v,xy}_{i+1/2,j+1/2,k} = \mu^n_{i+1/2,j+1/2,k}\left(\frac{u^n_{i+1/2,j+1,k} - u^n_{i+1/2,j+1/2,k}}{\Delta y} + \frac{v^n_{i+1,j+1/2,k} - u^n_{i,j+1/2,k}}{\Delta x}\right), \tag{2.26d}$$

$$T^{v,xz}_{i+1/2,j,k+1/2} = \mu^n_{i+1/2,j,k+1/2}\left(\frac{u^n_{i+1/2,j,k+1} - u^n_{i+1/2,j,k}}{\Delta z} + \frac{w^n_{i+1,j,k+1/2} - u^n_{i,j,k+1/2}}{\Delta x}\right), \tag{2.26e}$$

$$T^{v,yz}_{i,j+1/2,k+1/2} = \mu^n_{i,j+1/2,k+1/2}\left(\frac{w^n_{i,j+1,k+1/2} - w^n_{i,j,k+1/2}}{\Delta y} + \frac{v^n_{i,j+1/2,k+1} - v^n_{i,j+1/2,k}}{\Delta z}\right). \tag{2.26f}$$

Notice that the viscous stress tensor is symmetric.

Plugging in equations (2.26) into equations (2.25) results in second-order central differencing of the diffusion terms:

$$
\begin{aligned}
(D_x)^n_{i+1/2,j,k} &= 2\mu^n_{i+1,j,k}\frac{u^n_{i+3/2,j,k}-u^n_{i+1/2,j,k}}{\Delta x^2} - 2\mu^n_{i,j,k}\frac{u^n_{i+1/2,j,k}-u^n_{i-1/2,j,k}}{\Delta x^2} + \\
&\mu^n_{i+1/2,j+1/2,k}\left(\frac{u^n_{i+1/2,j+1,k}-u^n_{i+1/2,j,k}}{\Delta y^2} + \frac{v^n_{i+1,j+1/2,k}-v^n_{i,j+1,k}}{\Delta y \Delta x}\right) - \mu^n_{i+1/2,j-1/2,k} \\
&\left(\frac{u^n_{i+1/2,j,k}-u^n_{i+1/2,j-1,k}}{\Delta y^2} + \frac{v^n_{i+1,j-1/2,k}-v^n_{i,j-1/2,k}}{\Delta y \Delta x}\right) + \mu^n_{i+1/2,j,k+1/2} \\
&\left(\frac{u^n_{i+1/2,j,k+1/2}-u^n_{i+1/2,j,k}}{\Delta z^2} + \frac{w^n_{i+1,j,k+1/2}-w^n_{i,j,k+1/2}}{\Delta z \Delta x}\right) - \mu^n_{i+1/2,j,k-1/2} \\
&\left(\frac{u^n_{i+1/2,j,k}-u^n_{i+1/2,j,k-1}}{\Delta z^2} + \frac{w^n_{i+1,j,k-1/2}-w^n_{i,j,k-1/2}}{\Delta z \Delta x}\right).
\end{aligned}
\tag{2.27}
$$

The discretized form of y and z components of the diffusion terms are given in Appendix A.

Now, we use the midpoint rule to approximate the advection terms in (2.10):

$$
\begin{aligned}
(A_x)^n_{i+1/2,j,k} = \frac{1}{\Delta x \Delta y \Delta z}&[[(uu)_{i+1,j,k} - (uu)_{i,j,k}]\Delta y \Delta z + [(uv)_{i+1/2,j+1/2,k} - \\
&(uv)_{i+1/2,j-1/2,k}]\Delta x \Delta z + [(uw)_{i+1/2,j,k+1/2} - (uw)_{i+1/2,j,k-1/2}]\Delta x \Delta y],
\end{aligned}
\tag{2.28a}
$$

$$
\begin{aligned}
(A_y)^n_{i,j+1/2,k} = \frac{1}{\Delta x \Delta y \Delta z}&[[(uv)_{i+1/2,j+1/2,k} - (uv)_{i-1/2,j+1/2,k}]\Delta y \Delta z + [(vv)_{i,j+1,k} - \\
&(vv)_{i,j,k}]\Delta x \Delta z + [(wv)_{i,j+1/2,k+1/2} - (wv)_{i,j,k-1/2}]\Delta x \Delta y],
\end{aligned}
\tag{2.28b}
$$

$$
\begin{aligned}
(A_z)^n_{i,j,k+1/2} = \frac{1}{\Delta x \Delta y \Delta z}&[[(uw)_{i+1/2,j,k+1/2} - (uw)_{i-1/2,j,k+1/2}]\Delta y \Delta z + [(vw)_{i,j+1/2,k-1/2} - \\
&(vw)_{i,j-1/2,k+1/2}]\Delta x \Delta z + [(ww)_{i,j,k+1} - (ww)_{i,j,k}]\Delta x \Delta y].
\end{aligned}
\tag{2.28c}
$$

The velocities in equations (2.28) can be approximated by different methods depending on the selected scheme. In second-order central differencing the velocities at the boundary of control volume can be interpolated as:

$$(A_x)^n_{i+1/2,j,k} = \frac{1}{\Delta x}[(\frac{u^n_{i+3/2,j,k} + u^n_{i+1/2,j,k}}{2})^2 - (\frac{u^n_{i+1/2,j,k} + u^n_{i-1/2,j,k}}{2})^2] +$$
$$\frac{1}{\Delta y}[(\frac{u^n_{i+1/2,j+1,k} + u^n_{i+1/2,j,j}}{2})(\frac{v^n_{i+1,j+1/2,k} + v^n_{i,j+1/2,k}}{2}) -$$
$$(\frac{u^n_{i+1/2,j,k} + u^n_{i+1/2,j-1,k}}{2})(\frac{v^n_{i+1,j-1/2,k} + v^n_{i,j-1/2,k}}{2})] + \frac{1}{\Delta z}[(\frac{u^n_{i+1/2,j,k} + u_{i+1/2,j,k+1}}{2})$$
$$(\frac{w^n_{i+1,j,k+1/2} + w^n_{i,j,k+1/2}}{2}) - (\frac{u^n_{i+1/2,j,k} + u^n_{i+1/2,j,k-1}}{2})(\frac{w^n_{i,j,k-1/2} + w^n_{i+1,j,k-1/2}}{2})], \tag{2.29}$$

The discretized form of y and z components of the advection terms are given in Appendix B.

A third-order QUICK scheme can be implemented as:

$$u_{i,j,k} = \begin{cases} \frac{1}{8}(3u_{i+1/2,j,k} + 6u_{i-1/2,j,k} - u_{i-3/2,j,k}), & \text{if } \frac{1}{2}(u_{i-1/2,j,k} + u_{i+1/2,j,k}) > 0 \\ \\ \frac{1}{8}(3u_{i-1/2,j,k} + 6u_{i+1/2,j,k} - u_{i+3/2,j,k}), & \text{if } \frac{1}{2}(u_{i-1/2,j}, k + u_{i+1/2,j,k}) < 0 \end{cases} \tag{2.30}$$

similarly, for the v and w terms.

Substituting the discretized form of diffusion terms D (equation (2.27)) and the advection terms A (equation (2.29)) into equations (2.20) results in the temporary velocity field. The pressure field is resolved by solving the Poison equation, equation (2.22). With both the temporary velocity field and the pressure field known, the velocity can be corrected by equation (2.21). Therefore, the final velocity field is resolved for the entire domain.

Defining the ghost points simplifies the implementation of velocity boundary conditions. For instance, a linear interpolation of velocities at the bottom boundary gives:

$$v_{i,j-1/2,k} = \frac{1}{2}(v_{i,j-1,k} + v_{i,j+1/2,k}). \tag{2.31}$$

The boundary condition at the bottom of the domain is noslip, which requires the velocity at the boundary to be zero. Therefore:

$$v_{i,j-1/2,k} = -v_{i,j+1/2,k}. \tag{2.32}$$

2.1.2 Front Tracking Method

Numerical simulation of multiphase flow requires a method to identify and refer to each phase. The front-tracking method is a numerical technique to capture a moving interface. The interface is represented by marker points connected to each other to form elements. In a two-dimensional problem, the marker points are connected to form one-dimensional elements. Whereas, in a three-dimensional problem the front elements are triangular. The connectivity between the neighboring points and elements must be maintained through the entire interface. There are three major steps required for the successful implementation of the front tracking method. The structure of the interface and appropriate setting of the connectivity, the communication between the front and the grid to obtain the correct flow properties, and advecting the front. These steps are elaborated upon as follows.

We represent the three-dimensional interfaces using unstructured triangular meshes. Consider a flat interface as shown in figure 2.4. The front comprises points connected by elements. The coordinates of the points are stored for each point. The elements carry most of the front information including the connectivity. Each element knows about its surrounding points and the surrounding elements. The connectivity of points and elements can be set either in clockwise or anticlockwise directions. This direction defines the outside and the inside of the elements. All the elements of an interface must follow the same direction. For instance, in figure 2.4 the neighboring points of element 1 are set in a anticlockwise

direction as $[1, nps+2, nps+1]$, and as the periodicity implies the neighboring elements of element 1 are [2, nes+2, nes]. Moreover, the physical information of the interface such as surface tension is stored in the front elements. The proper implementation of the front structure and correct setting of the connectivity is crucial for success in the front tracking method.

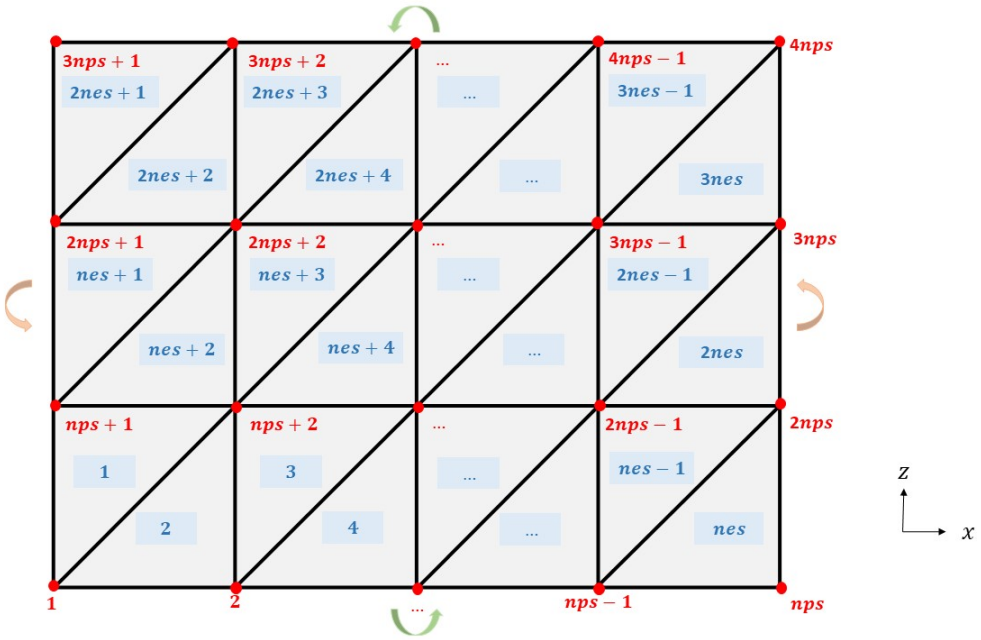

Figure 2.4: The front points range from 1 to $4nps$, shown by red. The front elements range from 1 to $3nes$. Each element is aware of the neighboring points and neighboring elements. The periodic boundary conditions in x and z directions are implemented through connectivity. The arrows represent the periodicity.

After defining the structure of the interface, the next step is to establish a smooth communication of data between the front and the grid. To do this, first, the interface must be located on the fixed grid. For periodic interfaces, the closest fixed grid point to the left of the front point x_f is given by:

$$i = FLOOR\left(MOD(x_f, L_x) \times \frac{N_x}{L_x}\right), \tag{2.33}$$

provided that $i = 0$ corresponds to $x = 0$. Here, N_x is the total number of grid points in x direction, and L_x is the length of the domain. The $FLOOR$ operation rounds down to the operand to the closest integer value. And $MOD(x_f, L_x)$

returns the remainder of x_f divided by L_x. Notice that in periodic fronts the endpoint of one period is connected to the first point of the next period.

After identifying the closest grid points to a given location on the front, we can interpolate the variables on the fixed grid to the front using:

$$\phi_f^l = \Sigma_{i,j,k} W_{i,j,k}^l \phi_{i,j,k}, \tag{2.34}$$

where ϕ_f^l is a quantity on the front at location l. $\phi_{i,j,k}$ is the same quantity on the fixed grid. And $W_{i,j,k}$ is the weight of the interpolation.

The interpolation of values from the front to the fixed grid is represented by:

$$\phi_{i,j,k} = \Sigma_l \phi_f^l W_{i,j,k}^l \frac{\Delta A_l}{\Delta x \Delta y \Delta z}, \tag{2.35}$$

where ΔA_l is the element surface area, $\Delta x, \Delta y, \Delta z$ are grid spacings, and $W_{i,j,k}^l$ is the weighting.

The summations are over the closest grid points to a specific front point as shown in figure 2.5. The number of the points used for interpolation depends on the smoothness of the weighting method. The weight for the grid point (i, j, k) for interpolation to $\mathbf{x}_f^l = (x_f^l, y_f^l, z_f^l)$ is:

$$W_{i,j,k}^l(\mathbf{x}_f^l) = d(r_x)d(r_y)d(r_z), \tag{2.36}$$

where $r_x = \dfrac{x_f^l - i\Delta x}{\Delta x}$ is the scaled distance between x_f^l and the grid line located at x_i provided that $i = 0$ corresponds to $x = 0$. Likewise, the expressions for $d(r_y)$ and $d(r_z)$ can be obtained.

We use the Peskin's distribution function (equation 2.37) for weightings, which is a smooth distribution function and uses a total of 64 points (8 points in each direction) for interpolations.

$$d(r) = \begin{cases} \frac{1}{4}(1 + cos(\frac{\pi r}{2})), & \text{if } |r| < 2 \\ \\ 0, & \text{if } |r| \geq 2 \end{cases} . \tag{2.37}$$

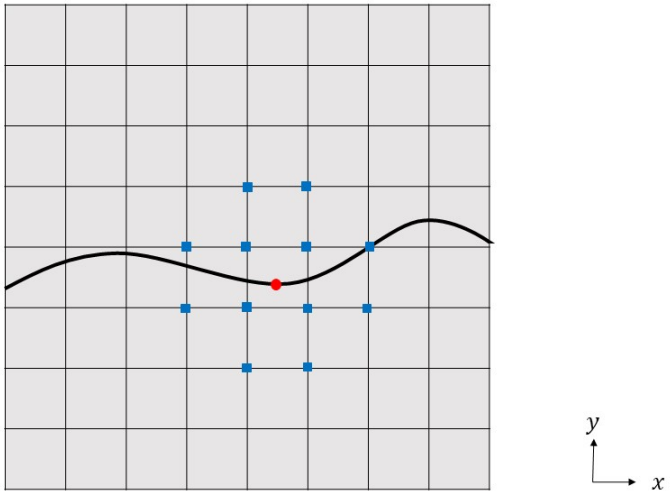

Figure 2.5: The interface is located on the fixed grid (the black line). The variables are interpolated for the front point (the red point) from 4 grid points in each direction (the blue points) using the smooth distribution function of equation (2.37). The figure is inspired by [2].

In the front tracking method, the interface is moved with the velocity of the fluid. We interpolate the velocity from the grid to the front using equation (2.34). Once the velocities at the front points are known, we advect the front points using:

$$\mathbf{X}_f^{n+1} = \mathbf{X}_f^n + \mathbf{V}_f^n \Delta t, \tag{2.38}$$

where $\mathbf{X}_f^{n+1}$ denotes the front position at time step $n+1$, $\mathbf{X}_f^n$ is the front position at time step n, $\mathbf{V}_f^n$ is the velocity of front points obtained by interpolation from the grid, and Δt is the time step.

In section 2.1.1 we mentioned that the one-fluid approach solves the governing equations for the entire domain. The front tracking method distinguishes the two immiscible fluids by referring to the location of the front and establishing an indicator function also known as the color function. The indicator function takes values ranging from 0 to 1 with zero representing the gas and one representing the liquid phase. (equation 2.39). A smooth jump occurs in the value of the indicator function. As we proceed from liquid to gas phase, the indicator function smoothly changes from 1 to 0.

$$I = \begin{cases} 1, & \text{if liquid} \\ \\ 0, & \text{if gas} \end{cases} . \tag{2.39}$$

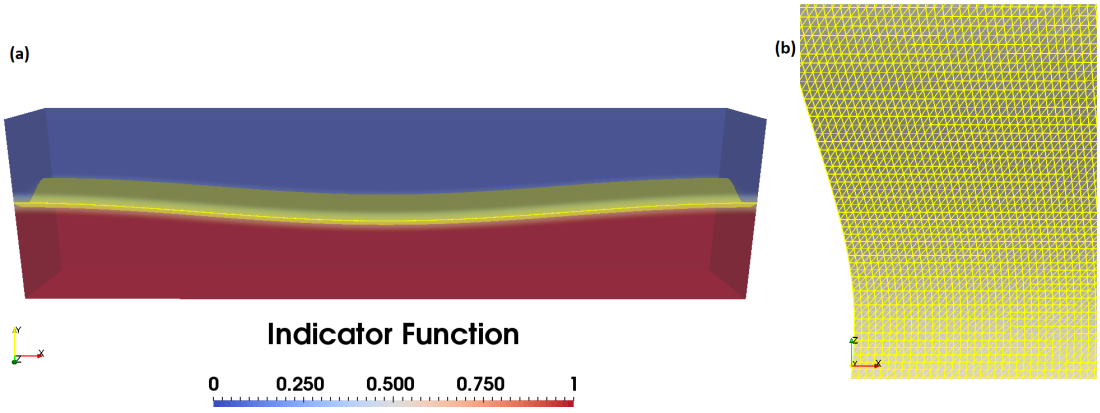

Figure 2.6: **(a)** Indicator Function in a three-dimensional domain. The red region, where $I = 1$ represents the liquid phase. The blue region, where $I = 0$ represents the gas phase. The yellow surface indicates the interface. **(b)** Triangular unstructured grid of the interface.

The fluid properties such as density and viscosity are updated according to the color function at the end of the time step:

$$\rho = \rho_{liquid} I + \rho_{gas}(1 - I), \tag{2.40}$$

$$\mu = \mu_{liquid} I + \mu_{gas}(1 - I). \tag{2.41}$$

The marker function $I(\mathbf{x})$ is constructed using the gradient of the jump in the marker function across the interface. The gradient of indicator function is expressed as:

$$\nabla \mathbf{I} = \int \Delta \mathbf{I} \mathbf{n} \delta(\mathbf{x} - \mathbf{x}_f) ds, \tag{2.42}$$

where $\Delta \mathbf{I}$ is the jump in the value of indicator function across the interface (a constant for each interface). This value is then interpolated onto the grid using equation(2.34). The distribution of the indicator function gradient on staggered grid results in a Poisson equation, the solution of which is the indicator function.

In order to obtain an expression for the marker function $I(i, j, k)$ we average the gradients of indicator function on the grid shown in figure 2.7 using the second-order central differencing scheme, which results in a Poisson equation:

$$\nabla^2 I = \nabla \cdot (\nabla I), \tag{2.43}$$

$$\begin{aligned} &\frac{I_{i+1,j,k} + I_{i-1,j,k} - 2I_{i,j,k}}{\Delta x^2} + \frac{I_{i,j+1,k} + I(i, j-1, k) - 2I_{i,j,k}}{\Delta y^2} + \\ &\qquad \frac{I_{i,j,k+1} + I_{i,j,k-1} - 2I_{i,j,k}}{\Delta z^2} = \\ &\frac{(\frac{\partial I}{\partial x})_{i+1/2,j,k} - (\frac{\partial I}{\partial x})_{i-1/2,j,k}}{\Delta x} + \frac{(\frac{\partial I}{\partial y})_{i,j+1/2,k} - (\frac{\partial I}{\partial y})_{i,j-1/2,k}}{\Delta y} + \\ &\qquad \frac{(\frac{\partial I}{z})_{i,j,k+1/2} - (\frac{\partial I}{\partial z})_{i,j,k-1/2}}{\Delta z}. \end{aligned} \tag{2.44}$$

Equation (2.44) can be solved with one of the two methods mentioned in section 2.1.1, the SOR method, or the multigrid methods of HYPRE library. In terms of programming, the indicator function Poisson solvers require a lower residual (in the order of $1e-9$) compared to the Poisson pressure solver (in the order of $1e-6$) to capture the interface smoothly. The residual can be lower depending on the curvature and the complexity of the interface.

Notice that figure 2.4 shows the initial condition for a flat interface. The coordinates of the front points are updated as the front is advected using the interpolated velocity from the main grid. Accordingly, front elements experience changes in size and shape as the interface evolves.

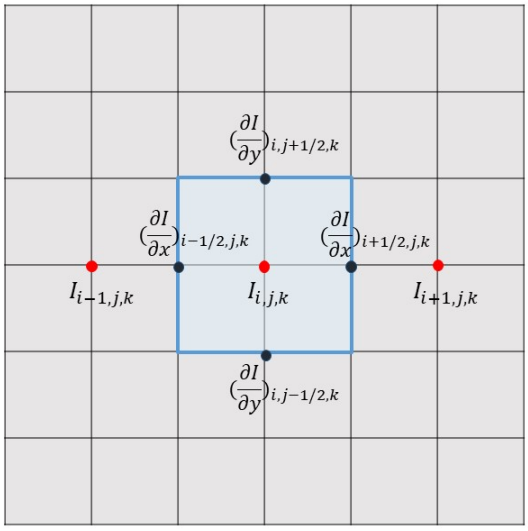

Figure 2.7: The plot of marker function and its gradients on a staggered grid.The figure is inspired by [2].

2.1.3 Continuous Surface Force (CSF) Method

The role of surface tension is crucial in both falling liquid films and multiphase flow. In the one-fluid approach, the surface tension forces are added as a body force to the discrete version of the Navier-Stokes equations as explained in section 2.1.1. In this section, we discuss computing the surface tension in the front tracking method and distributing it on the fixed grid. The Continuous Surface Force (CSF) is used to attribute surface tension force values to each front point. the net force due to surface tension is proportional to the curvature of the interface. The force on a surface segment is:

$$\delta f_e = \int_{\Delta A} \sigma \kappa \mathbf{n} da, \tag{2.45}$$

where σ is the surface tension coefficient and κ is the curvature of a three-dimensional front.

Assuming a constant surface tension coefficient and using the Stokes theorem, we convert the area integral to the line integral along the edges of the segment:

$$\delta f_e = \sigma \int_{\Delta A} (\mathbf{n} \times \nabla) \times \mathbf{n} da = \sigma \oint_C \mathbf{p} dl, \tag{2.46}$$

here, $\mathbf{p} = \mathbf{t} \times \mathbf{n}$, where $\mathbf{t}$ is a vector tangent to the edge of the elemen, $\mathbf{n}$ is a normal vector to the surface, ΔA is the element area and C is element boundary. The surface segment we work with consists of a third of all the elements connected to a given front point. The coordinates of this element corners are given as $\mathbf{x}_1, \mathbf{x}_2, \mathbf{x}_3$ so the element centroid is:

$$\mathbf{x}_c = \frac{1}{3}(\mathbf{x}_1 + \mathbf{x}_2 + \mathbf{x}_3), \tag{2.47}$$

while the midpoints of the sides are:

$$\mathbf{x}_{12} = \frac{1}{2}(\mathbf{x}_1 + \mathbf{x}_2), \mathbf{x}_{23} = \frac{1}{2}(\mathbf{x}_2 + \mathbf{x}_3), \mathbf{x}_{13} = \frac{1}{2}(\mathbf{x}_1 + \mathbf{x}_3). \tag{2.48}$$

The normal to the element is found by:

$$\mathbf{n}_e = \frac{\Delta \mathbf{x}_{12} \times \Delta \mathbf{x}_{13}}{|\Delta \mathbf{x}_{12} \times \Delta \mathbf{x}_{13}|}. \tag{2.49}$$

Since the force on the side connecting $\mathbf{x}_1$ and $\mathbf{x}_{12}$ are canceled by the force from the other elements surrounding the segment and the force on the side connecting $\mathbf{x}_1$ and $\mathbf{x}_{31}$ is canceled in a similar manner, we only need to consider the lines

connecting $\mathbf{x}_{12}$ and $\mathbf{x}_{31}$ to the center (see figure 2.8). Pay attention that such cancellation of forces occurs only when the segment is surrounded entirely by the other elements. In the case of a surface front, the boundary elements are not entirely bordered by the other elements and thus, the surface tension force arising from them must be taken into account. Evaluation of the integral in equation (2.46) over the first line segment is:

$$\int_{\Delta C} \mathbf{p} dl = \mathbf{p}_1 \Delta s_1 = \mathbf{n}_e \times \frac{\mathbf{x}_c - \mathbf{x}_{12}}{\Delta s_1} \Delta s_1 = \mathbf{n}_e \times (\mathbf{x}_c - \mathbf{x}_{12}). \tag{2.50}$$

The net surface tension force for point 1 results from the contribution of $\mathbf{p}_1$and $\mathbf{p}_2$:

$$\delta \mathbf{f}_{1e} = \mathbf{p}_1 \Delta s_1 + \mathbf{p}_2 \Delta s_2 = \frac{1}{2} \mathbf{n}_e \times \Delta \mathbf{x}_{32}. \tag{2.51}$$

Similarly for the other points:

$$\delta \mathbf{f}_{2e} = \frac{1}{2} \mathbf{n}_e \times \Delta \mathbf{x}_{13}, \delta \mathbf{f}_{3e} = \frac{1}{2} \mathbf{n}_e \times \Delta \mathbf{x}_{21}. \tag{2.52}$$

As we mentioned before, properties such as surface tension and gradients of indicator function are stored in front points. Therefore, the communication between front to grid and grid to the front is essential to transfer these data. Both communications are carried out by interpolation. The smoother the interpolation function, the more accurate the data transfer. A smooth weighting function developed by Peskin (1977) is used in the current work as mentioned in 2.1.2. Using equation (2.34) we interpolate the surface tension from the front points to the grid points.

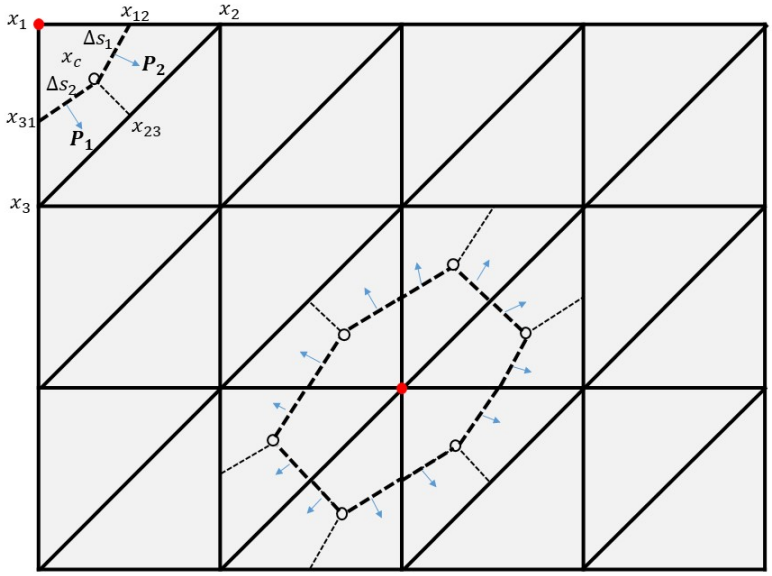

Figure 2.8: Surface tension force distribution on the front points. One-third of each element contributes to the calculation of surface tension force. The integral in equation (2.46) is evaluated over the element segment.The figure is inspired by [2].

2.2 Turbulence

LES/DNS of turbulent flow is known to demand highly accurate numerical methods to capture the physics. High-order numerical methods can extremely increase computational costs. On the other hand, using numerical techniques introduces a loss of accuracy due to several factors such as accumulated errors, boundary conditions, and failure of conservation properties, which leads to spurious oscillations (wiggles) at small scales. Wiggles can be controlled by using a highly refined mesh; however, this is not a practical method because it is overly demanding in computational resources. Using a specific artificial damping term, or filtering the equations are some feasible, but not necessarily straight-forward methods to control spurious oscillations. In this section, first, we present the conventional Spectral Vanishing Viscosity (SVV) method. Then, we introduce an extension of the Spectral Vanishing Viscosity (SVV) method from spectral space to finite-differences with higher-order discretizations. We use the extension of SVV to

finite-differences to approximate the second derivative terms in the Navier-Stokes equations.

2.2.1 Spectral Vanishing Viscosity (SVV) Method

E. Tadmor was the first to introduce the concept of SVV. In this section, we will review the application of the conventional SVV method to the one-dimensional inviscid Burgers equation [7].

$$\frac{\partial}{\partial t}u(x,t) + \frac{\partial}{\partial x}(\frac{u^2(x,t)}{2}) = 0, \tag{2.53}$$

Spontaneous jump discontinuities may develop in the solutions of this problem, leading to a class of weak solutions. In order to select the physically relevant solution we introduce an entropy condition in the form:

$$\frac{\partial}{\partial x}(\frac{u^2(x,t)}{2}) + \frac{\partial}{\partial x}(\frac{u^3(x,t)}{3}) \leq 0. \tag{2.54}$$

Tadmor [6] proposed the idea of SVV by adding a controlled amount of dissipation, which satisfies the entropy condition and maintains the spectral accuracy at the same time. The introduced dissipation term is based on viscosity solutions of nonlinear Hamiltonian-Jacobi equations [7]:

$$\frac{\partial}{\partial t}u(x,t) + \frac{\partial}{\partial x}(\frac{u^2(x,t)}{2}) = \epsilon\frac{\partial}{\partial x}[Q_\epsilon\frac{\partial u}{\partial x}], \tag{2.55}$$

where ϵ is a viscosity amplitude and Q_ϵ is a viscosity kernel.

The discrete form of equation (2.55) in spectral space, retaining N modes is:

$$\frac{\partial}{\partial t}u(x,t) + \frac{\partial}{\partial x}[P_N(\frac{u^2(x,t)}{2})] = \epsilon\frac{\partial}{\partial x}[Q_N * \frac{\partial u_N}{\partial x}], \tag{2.56}$$

where P_N is a projection operator. Q_N is a viscosity kernel, which only activates for high wavenumbers. And $*$ states convolution. The right-hand side of equation (2.56) in Fourier space can be evaluated as:

$$\epsilon \frac{\partial}{\partial x}[Q_N * \frac{\partial u_N}{\partial x}] = -\epsilon \Sigma_{M \leq |k| \leq N} k^2 \hat{Q}_k(t) \hat{u}_k(t) e^{ikx}, \tag{2.57}$$

where k is the wavenumber, N is the number of Fourier modes, and M is the wavenumber above which SVV activates. The kernel originally used by Tadmor [6] is:

$$\hat{Q}_k = \begin{cases} 0 & |k| \leq M \\ & \\ 1 & |k| > M \end{cases}. \tag{2.58}$$

Notice that the viscosity amplitude vanishes ($\epsilon \to 0$) for the wavenumbers smaller than M, which explains the vanishing viscosity in the title of this method.

G-S. Karamanos *et al.* [7] applied the SVV method to two-dimensional and three-dimensional Navier-Stokes equations using a smooth kernel in the case of single-phase turbulent channel flows. We study this test case in section 4.2.

Since the numerical tool we developed is based on the finite-volume method, we cannot directly implement the conventional SVV. Therefore, we will use an extension of the SVV method from the spectral space to finite-differences.

2.2.2 Extension of SVV to Finite-differences

E. Lamballais *et al.* [8] introduced a highly-accurate finite-difference scheme to compute second derivative terms in the Navier-Stokes equation. This scheme does not use any upwinding, damping, or filtering operators as opposed to popular turbulence modeling schemes such as implicit LES and Spectral Methods. The

finite-difference scheme used to compute second derivative terms in Navier-Stokes equations includes extra dissipation in the viscous terms. This method is shown to behave like a spectral vanishing viscosity operator [19, 20].

In order to compare the finite-difference extension of SVV with conventional SVV, we use the compact differences formulation presented by Lele [1] to approximate the first derivative and the second derivative terms. The first derivative terms can be approximated by:

$$\beta u'_{i-2} + \alpha u'_{i-1} + u'_i + \alpha u'_{i+1} + \beta u'_{i+2} = a\frac{u_{i+1} - u_{i-1}}{2\Delta x} + b\frac{u_{i+2} - u_{i-2}}{4\Delta x} + c\frac{u_{i+3} - u_{i-3}}{6\Delta x}, \tag{2.59}$$

where $u_i = x_i$ and $u'_i = u'(x_i)$ are values of function u and its first derivative at node $x_i = (i-1)\Delta x$, with Δx being the uniform mesh spacing. The coefficient set (α, β, a, b, c) are derived by matching the Taylor Series of coefficient of various orders. The coefficients are constrained by the conditions in equations (2.60) [1].

$$a + b + c = 1 + 2\alpha + 2\beta \text{ (second order condition)}, \tag{2.60a}$$

$$a + 2^2 b + 3^2 c = 2\frac{3!}{2!}(\alpha + 2^2\beta) \text{ (fourth order condition)}, \tag{2.60b}$$

$$a + 2^4 b + 3^4 c = 2\frac{5!}{4!}(\alpha + 2^4\beta) \text{ (sixth order condition)}, \tag{2.60c}$$

$$a + 2^6 b + 3^6 c = 2\frac{7!}{6!}(\alpha + 2^6\beta) \text{ (eigth order condition)}, \tag{2.60d}$$

$$a + 2^8 b + 3^8 c = 2\frac{9!}{8!}(\alpha + 2^8\beta) \text{ (tenth order condition)}. \tag{2.60e}$$

The coefficients of tridiogonal ($\beta = 0$) and pentadiogonal ($\beta \neq 0$) schemes to approximate the spectral-like behavior of the first derivatives are given in Table 2.1 .

The following finite-difference scheme can be used to discretize the second derivative term in the Navier-Stokes as:

Table 2.1: Coefficients of first derivative compact difference formulation according to Lele [1].

Order of Accuracy	α	β	a	b	c
4^{th}	$\frac{1}{4}$	0	$\frac{3}{2}$	0	0
6^{th}	$\frac{1}{3}$	0	$\frac{14}{9}$	$\frac{1}{9}$	0
8^{th}	$\frac{3}{8}$	0	$\frac{25}{16}$	$\frac{1}{5}$	0
10^{th}	$\frac{1}{2}$	$\frac{1}{20}$	$\frac{17}{12}$	$\frac{101}{150}$	$\frac{1}{100}$

$$\beta u''_{i-2} + \alpha u''_{i-1} + u''_i + \alpha u''_{i+1} + \beta u''_{i+2} = a\frac{u_{i+1} - 2u_i + u_{i-1}}{\Delta x^2} + b\frac{u_{i+2} - 2u_i u_{i-2}}{4\Delta x^2} + c\frac{u_{i+3} - 2u_i u_{i-3}}{9\Delta x^2} + d\frac{u_{i+4} - 2u_i u_{i-4}}{16\Delta x^2}, \tag{2.61}$$

where $u_i = x_i$ and $u''_i = u''(x_i)$ are values of function u and its second derivative at node $x_i = (i-1)\Delta x$, with Δx being the uniform mesh spacing. The coefficient set $(\alpha, \beta, a, b, c, d)$ ensures up to tenth-order accuracy by satisfying the conditions in equations (2.62) [19, 21].

$$a + b + c + d = 1 + 2\alpha + 2\beta \text{ (second order condition)}, \tag{2.62a}$$

$$a + 2^2 b + 3^2 c + 4^2 d = \frac{4!}{2!}(\alpha + 2^2\beta) \text{ (fourth order condition)}, \tag{2.62b}$$

$$a + 2^4 b + 3^4 c + 4^4 d = \frac{6!}{4!}(\alpha + 2^4\beta) \text{ (sixth order condition)}, \tag{2.62c}$$

$$a + 2^6 b + 3^6 c + 4^6 d = \frac{8!}{6!}(\alpha + 2^6\beta) \text{ (eigth order condition)}, \tag{2.62d}$$

$$a + 2^8 b + 3^8 c + 4^8 d = \frac{10!}{8!}(\alpha + 2^8\beta) \text{ (tenth order condition)}. \tag{2.62e}$$

The coefficients of schemes approximating the second derivative terms are given in Table 2.2.

Table 2.2: Coefficients of second derivative compact difference formulation according to Lele [1].

Order of Accuracy	α	β	a	b	c
4^{th}	$\frac{1}{10}$	0	$\frac{6}{5}$	0	0
6^{th}	$\frac{2}{11}$	0	$\frac{12}{11}$	$\frac{3}{11}$	0
8^{th}	$\frac{344}{1179}$	$\frac{23}{2358}$	$\frac{320}{393}$	$\frac{310}{393}$	0
10^{th}	$\frac{344}{899}$	$\frac{43}{1798}$	$\frac{1065}{1798}$	$\frac{1038}{899}$	$\frac{79}{1798}$

The resolution characteristics of different schemes can be compared by a modified wavenumber in the form of:

$$k'(k)\Delta x = \frac{a\sin(k\Delta x) + \frac{b}{2}\sin(2k\Delta x) + \frac{c}{3}\sin(3k\Delta x)}{1 + 2\alpha\cos(k\Delta x) + 2\beta\cos(2k\Delta x)}. \tag{2.63}$$

A modified square wave number k'' in Fourier space is related to the actual wavenumber k by:

$$k''(k)\Delta x^2 = \frac{2a[1-\cos(k\Delta x)] + \frac{b}{2}[1-\cos(2k\Delta x)] + \frac{2c}{9}[1-\cos(3k\Delta x) + \frac{d}{8}[1-\cos(4k\Delta x)]}{1 + 2\alpha\cos(k\Delta x) + 2\beta\cos(2k\Delta x)}, \tag{2.64}$$

where $k \in [0, k_c]$ is the actual wave number. And $k_c = \dfrac{\pi}{\Delta x}$ is the cutoff wave number associated with the grid size. The exact differentiation for the first and second derivatives are given by $k'(k) = k$ and $k''(k) = k^2$, respectively.

The equations (2.63) and (2.64) can be used to compare the accuracy of the compact difference formulation compared to the conventional spectral method. The resolution Analysis and the error percentage compared to the traditional spectral discretization for first and second derivatives are given in figures 2.9 and 2.10 respectively. Notice that the resolution analysis is independent of the grid

specifications. Figures 2.9 and 2.10 indicate that the approximations in equations (2.59) and (2.67) can accurately mimic the spectral-like behavior using finite-differences. The tenth-order scheme covers the highest range of wavenumbers in a domain of $[0, \pi]$.

Moreover, Lele [1] indicated that selecting the coefficients as $(\alpha, \beta, a, b, c, d) = (2/11, 0, 12/11, 3/11, 0, 0)$ results is an optimal sixth-order SVV-like behavior. However, we showed in section 2.1.1 that we use a first-order accurate temporal and second-order accurate spatial scheme. Therefore, we propose a lower-order SVV-like polynomial.

According to Lele [1] a one-parameter family of fourth-order schemes is obtained by selecting the coefficients as:

$$a = \frac{4}{3}(1 - \alpha), \tag{2.65a}$$

$$b = \frac{1}{3}(-1 + 10\alpha), \tag{2.65b}$$

$$c = 0. \tag{2.65c}$$

As $\alpha \to 0$ this family approaches the fourth-order central difference scheme. For $\alpha = \frac{1}{10}$ the classical Padé scheme is obtained with $(\alpha, \beta, a, b, c, d) = (1/10, 0, 6/5, 0, 0, 0)$. The coefficients lead to the following polynomial:

$$\frac{1}{10}u''_{i-1} + u''_i + \frac{1}{10}u''_{i+1} = \frac{6}{5}\frac{u_{i+1} - 2u_i + u_{i-1}}{\Delta x^2}, \tag{2.66}$$

with truncation error of $-\frac{4}{6!}(11\alpha - 2)h^4 f^{(6)}$.

Moreover, the second derivative term in the Navier-Stokes on a standard staggered grid can be discretized as:

$$\alpha u''_{i-1} + u''_i + \alpha u''_{i+1} = 4a\frac{u_{i+1/2} - 2u_i + u_{i-1/2}}{\Delta x^2} + 4b\frac{u_{i+3/2} - 2u_i + u_{i-3/2}}{4\Delta x^2} + 4c\frac{u_{i+5/2} - 2u_i + u_{i-5/2}}{9\Delta x^2}. \tag{2.67}$$

And, the fourth-order SVV-like behavior on a cell-centered staggered grid is given by [1]:

$$a = \frac{3}{8}(3 - 10\alpha), \tag{2.68a}$$

$$b = \frac{1}{8}(46\alpha - 1), \tag{2.68b}$$

$$c = 0, \tag{2.68c}$$

with truncation error of $\frac{1}{640}(1 + 2\alpha)h^4 f^{(6)}$.

A standard Padé scheme on a cell-centered staggered grid corresponds to $(\alpha, a, b, c, d) = (1/46, 24/23, 0, 0, 0)$. Therefore, the fourth-order polynomial to approximate the second derivatives is:

$$\frac{1}{46}u''_{i-1} + u''_i + \frac{1}{46}u''_{i+1} = \frac{96}{23}\frac{u_{i+1/2} - 2u_i + u_{i-1/2}}{\Delta x^2}. \tag{2.69}$$

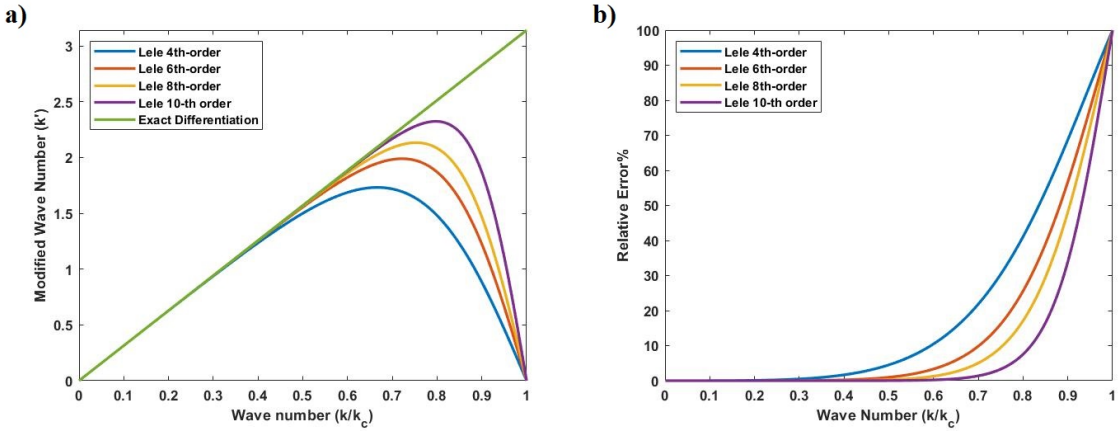

Figure 2.9: Resolution analysis for first derivative approximations. **(a)** The modified wavenumber vs. the normalized wavenumber. **(b)** The error percentage of higher-order polynomials compared to the spectral discretization.

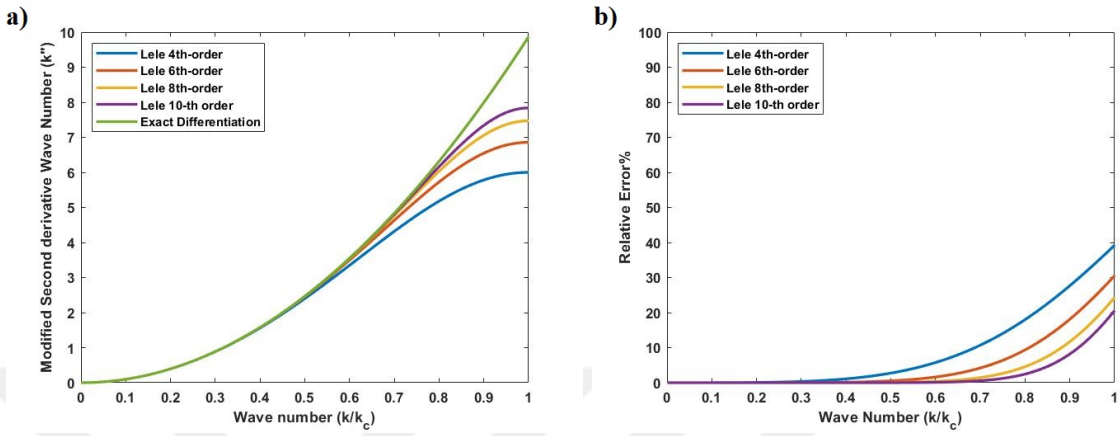

Figure 2.10: Resolution analysis for second derivative approximations. **(a)** The modified square wavenumber vs. the normalized wavenumber. **(b)** The error percentage of higher-order polynomials compared to the spectral discretization.

So far, we indicated that the finite-difference approximations are capable of resolving the spectral-like resolution covering up to nearly $\frac{2\pi}{3}$ of a domain of $[0, \pi]$. The next step to implementing Spectral Vanishing Viscosity method in finite-differences obtaining an SVV-like behavior by selecting an appropriate viscosity kernel.

According to Lamballais *et al.* [8] a fourth-order accuracy is obtained by choosing $\beta = 0$ and $d = 0$ and satisfying conditions (2.62a) and (2.62b). The two additional conditions are obtained using the cutoff wavenumber, $k''|_\pi = k''|_c$ and an intermediate scale such as $k\Delta x = \frac{2\pi}{3}$, meaning $k''|_{\frac{2\pi}{3}} = k''|_m$. We choose the two additional conditions in a way that the modified wave number at the selected scales matches the respective wavenumber of a SVV kernel [19, 21].

$$k''(k_c) = (1 + \frac{\nu_0}{\nu})k_c^2, \tag{2.70a}$$

$$k''(\frac{2k_c}{3}) = (1 + c_1\frac{\nu_0}{\nu})k_m^2, \tag{2.70b}$$

$$\tag{2.70c}$$

where $c_1 = 0.437$ is given by the SVV kernel at the intermediate scale. To obtain a better fit for the vanishing property of the SVV steep and sharp kernels are

given by $c_1 = 0.22$ and $c_1 = 0.055$ respectively. The value of $\frac{\nu_0}{\nu}$ controls the SVV-like behavior of the kernel. Therefore, $\frac{\nu_0}{\nu} = 0$ disables the SVV operator.

Combining the conditions (2.62a), (2.62b), (2.70a), and (2.70b) and solving a system of four equations leads to the following coefficients:

$$\alpha = \frac{64k_m''\Delta x^2 - 27k_c''\Delta x^2 - 96}{64k_m''\Delta x^2 - 54k_c''\Delta x^2 + 48}, \tag{2.71a}$$

$$a = \frac{54k_c''\Delta x^2 - 15k_c''\Delta x^2 k_m''\Delta x^2 + 12}{64k_m''\Delta x^2 - 54k_c''\Delta x^2 + 48}, \tag{2.71b}$$

$$b = \frac{192k_c''\Delta x^2 - 216k_c''\Delta x^2 + 24k_c''\Delta x^2 k_m''\Delta x^2 - 48}{64k_m''\Delta x^2 - 54k_c''\Delta x^2 + 48}, \tag{2.71c}$$

$$c = \frac{54k_c''\Delta x^2 - 9k_c''\Delta x^2 k_m''\Delta x^2 - 108}{64k_m''\Delta x^2 - 54k_c''\Delta x^2 + 48}. \tag{2.71d}$$

Furthermore, Lamballais *et al.* [8] obtained a sixth-order accurate scheme by setting $\beta = 0$ and $d = 0$, constrained by the (2.62a), (2.62b), (2.62c), and (2.70a) conditions leading to the following coefficients:

$$\alpha = \frac{272 - 45k_c''\Delta x^2}{416 - 90k_c''\Delta x^2}, \tag{2.72a}$$

$$a = \frac{48 - 135k_c''\Delta x^2}{1664 - 360k_c''\Delta x^2}, \tag{2.72b}$$

$$b = \frac{528 - 81k_c''\Delta x^2}{208 - 45k_c''\Delta x^2}, \tag{2.72c}$$

$$c = \frac{-432 + 63k_c''\Delta x^2}{1664 - 360k_c''\Delta x^2}. \tag{2.72d}$$

In addition, Deskos *et al.* [21] proposed a sixth-order accurate scheme setting $\beta = 0$ and conditioned by (2.62a), (2.62b), (2.70a), and (2.70b).

$$\alpha = \frac{1}{2} - \frac{320k_m''\Delta x^2 - 1296}{405k_c''\Delta x^2 - 640k_m''\Delta x^2 + 144}, \tag{2.73a}$$

$$a = -\frac{4329k_c''\Delta x^2/8 - 32k_m''\Delta x^2 - 140k_c''\Delta x^2 k_m''\Delta x^2 + 286}{405k_c''\Delta x^2 - 640k_m''\Delta x^2 + 144}, \tag{2.73b}$$

$$b = \frac{2115k_c''\Delta x^2 - 1792k_m''\Delta x^2 - 280k_c''\Delta x^2 k_m''\Delta x^2 + 1328}{405k_c''\Delta x^2 - 640k_m''\Delta x^2 + 144}, \tag{2.73c}$$

$$c = -\frac{7695k_c''\Delta x^2/8 + 288k_m''\Delta x^2 - 180k_c''\Delta x^2 k_m''\Delta x^2 - 2574}{405k_c''\Delta x^2 - 640k_m''\Delta x^2 + 144}, \tag{2.73d}$$

$$d = \frac{198k_c''\Delta x^2 + 128k_m''\Delta x^2 - 40k_c''\Delta x^2 k_m''\Delta x^2 - 736}{405k_c''\Delta x^2 - 640k_m''\Delta x^2 + 144}. \tag{2.73e}$$

In a similar manner, we derive a fourth-order accurate scheme with $\beta = 0$, $c = 0$, $d = 0$, and conditioned by (2.62a), (2.62b), and (2.70a).

$$\alpha = \frac{k_c''\Delta x^2 - \frac{16}{3}}{2k_c''\Delta x^2 - \frac{16}{3}}, \tag{2.74a}$$

$$a = \frac{4k_c''\Delta x^2}{6k_c''\Delta x^2 - 16}, \tag{2.74b}$$

$$b = \frac{8k_c''\Delta x^2 - \frac{144}{3}}{6k_c''\Delta x^2 - 16}. \tag{2.74c}$$

The extra dissipation introduced by the coefficients is represented by spectral viscosity as:

$$\nu_s = \nu(\frac{k'' - k^2}{k^2}), \tag{2.75}$$

where ν_s is the spectral viscosity and ν is the molecular viscosity.

The coefficients can be adjusted in a way that they mimic an SVV kernel that reads the conventional SVV kernel of Karamanos *et al.* [7]:

$$\nu_{SVV} = \begin{cases} 0 & m < mk_c \\ \\ \nu_0 \exp[-(\dfrac{k_c - k}{mk_c - k})^2] & m \leq k \leq k_c \end{cases} . \tag{2.76}$$

The standard SVV kernel reads the intermediate wavenumbers using $m = 0.3$.

Figure 2.11 plots the normalized spectral viscosity for sixth-order accurate SVV-like schemes against the normalized wavenumber. The Karamanos *et al.* kernel [7] is also plotted for reference. The sixth-order optimal scheme of Lele is highly under dissipative as it does not include the artificial dissipation introduced by viscosity. The sixth-order Deskos *et al.* scheme closely reads the Karamanos kernel covering almost $\frac{2}{3}$ of the wavenumbers. The value of $\frac{\nu_0}{\nu}$ can be adjusted to control the SVV behavior.

Figure 2.12 plots the normalized spectral viscosity for fourth-order accurate SVV-like schemes of Lele, Lamballais, and the scheme we derived in this note accordingly against the normalized wavenumber. The Karamanos *et al.* kernel [7] is also plotted for reference. The fourth-order scheme of Lele is highly under dissipative. Whereas, the fourth-order Lamballais *et al.* and SVV schemes closely read the Karamanos kernel covering almost $\frac{1}{3}$ of the wavenumbers. The SVV operator is adjusted using the $\frac{\nu_0}{\nu}$. We would like to avoid viscosity amplitudes larger than one to prevent extra dissipation and thus to guarantee numerical stability.

Finally, we indicate that our fourth-order SVV scheme is capable of precisely mimicking spectral-like behavior as indicated in figure 2.13. Fourth-order approximations of Lele and Lamballais are given for reference.

We apply the fourth-order SVV-like compact-difference formulation to the governing equations of the gas phase as follows. Notice that the fluid properties ρ, μ, and ν represent the properties of gas.

The momentum equation for incompressible flow with constant density and

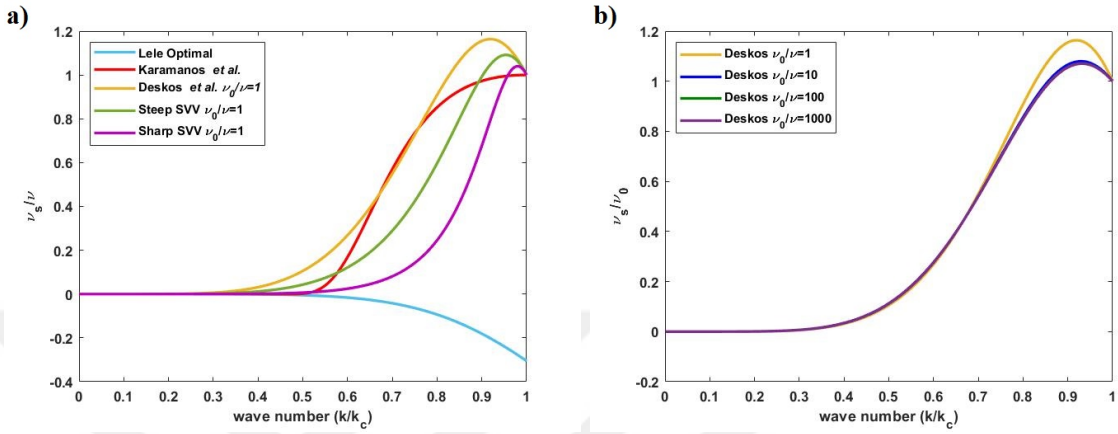

Figure 2.11: The plot of sixth-order accurate SVV-like schemes. **(a)** The normalized associated spectral viscosity of Lele optimal sixth-order accurate scheme, Karamanos *et al.* [7], Deskos *et al.* [21] sixth-order accurate with $c_1 = 0.437$, Steep SVV ($c_1 = 0.22$), Sharp SVV ($c_1 = 0.055$) plotted against the normalized wave number. **(b)** The SVV operator spectral viscosity scaled by the magnitude of $\frac{\nu_0}{\nu}$ plotted against the normalized wave number.

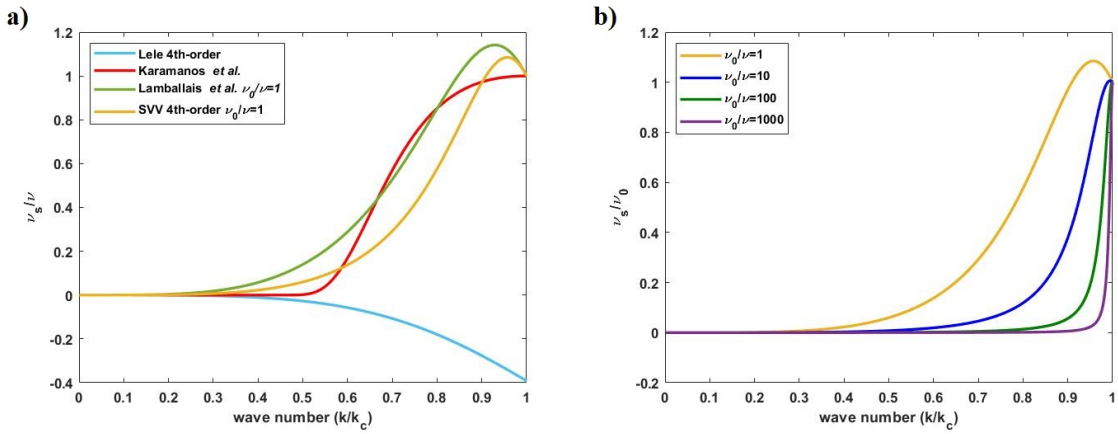

Figure 2.12: The plot of fourth-order accurate SVV-like schemes. **(a)** The normalized associated spectral viscosity of Lele fourth-order accurate scheme, Karamanos *et al.* [7], Lamballais *et al.* [8] fourth-order accurate, and the fourth-order SVV plotted against the normalized wave number. **(b)** The fourth-order SVV operator spectral viscosity scaled by the magnitude of $\frac{\nu_0}{\nu}$ plotted against the normalized wave number.

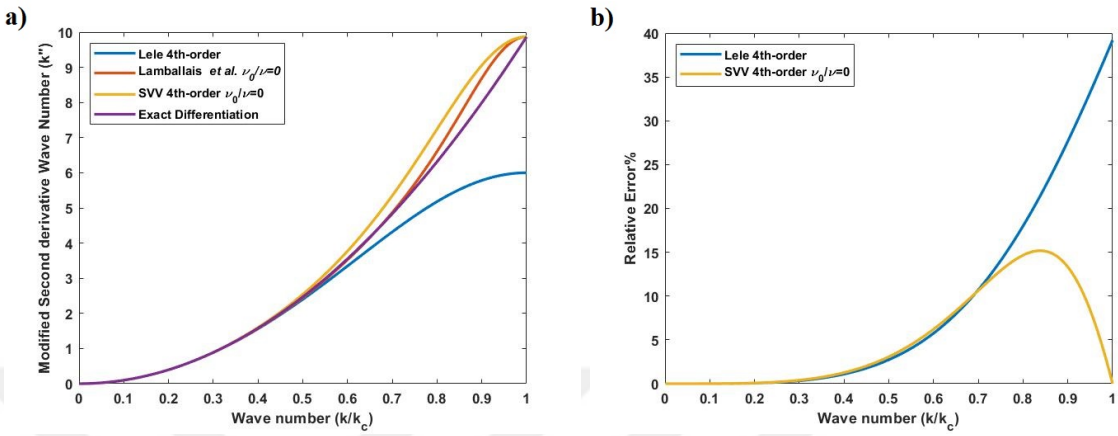

Figure 2.13: The plot of resolution analysis for SVV-like fourth-order schemes. **(a)** The modified square wave number vs. the normalized wave number. **(b)** The error percentage of SVV-like polynomials compared to the spectral discretization.

viscosity is given as:

$$\frac{\partial \mathbf{v}}{\partial t} + \mathbf{v}.\nabla\mathbf{v} = -\frac{\nabla P}{\rho} + \nu\nabla^2\mathbf{v} + \frac{\mathbf{f}}{\rho}, \tag{2.77}$$

where $\mathbf{A} = \mathbf{v}.\nabla\mathbf{v}$ and $\mathbf{D} = \nu\nabla^2\mathbf{v}$ are the advection and diffusion terms respectively. $\mathbf{f}$ represents the surface tension forces and ν is the molecular kinematic viscosity.

We apply the Spectral Vanishing Viscosity using a dissipation operator $\nu D = [\nu + \nu_s]\nabla^2\mathbf{v}$ in which ν_s is the spectral viscosity as given by equation (2.75). Therefore, the momentum equation can be rewritten as:

$$\frac{\partial \mathbf{v}}{\partial t} + \mathbf{v}.\nabla\mathbf{v} = -\frac{\nabla P}{\rho} + [\nu + \nu_s]\nabla^2\mathbf{v} + \frac{\mathbf{f}}{\rho}. \tag{2.78}$$

We apply a first-order time integration to the momentum equation:

$$\frac{\mathbf{v}^{n+1} - \mathbf{v}^n}{\Delta t} + \mathbf{A}_h^n = \frac{1}{\rho^n}(-\nabla_h p + \mathbf{D}_h^n + \mathbf{f}^n), \tag{2.79}$$

where $\mathbf{D}_h = [\nu + \nu_s]\nabla_h^2 \mathbf{v}$ is the diffusion term including the spectral viscosity.

We use the projection method introduced in section 2.1.1. The predictor and projection steps are obtained accordingly:

$$\frac{\mathbf{v}^* - \mathbf{v}^n}{\Delta t} = -\mathbf{A}_h^n + \frac{1}{\rho^n}(\mathbf{D}_h^n + \mathbf{f}_h^n), \tag{2.80a}$$

$$\frac{\mathbf{v}^{n+1} - \mathbf{v}^*}{\Delta t} = \frac{1}{\rho^n}(-\nabla_h p). \tag{2.80b}$$

The component-wise diffusion term is:

$$\mathbf{D}_x^n = [\nu + \nu_s](\frac{\partial^2 u}{\partial x^2} + \frac{\partial^2 u}{\partial y^2} + \frac{\partial^2 u}{\partial z^2}), \tag{2.81a}$$

$$\mathbf{D}_y^n = [\nu + \nu_s](\frac{\partial^2 v}{\partial x^2} + \frac{\partial^2 v}{\partial y^2} + \frac{\partial^2 v}{\partial z^2}), \tag{2.81b}$$

$$\mathbf{D}_z^n = [\nu + \nu_s](\frac{\partial^2 w}{\partial x^2} + \frac{\partial^2 w}{\partial y^2} + \frac{\partial^2 w}{\partial z^2}). \tag{2.81c}$$

We write equation (2.81) on the staggered grid as:

$$(\mathbf{D}_x^n)_{i+1/2,j,k} = [\nu + \nu_s]((u_x'')_{i+1/2,j,k} + (u_y'')_{i+1/2,j,k} + (u_z'')_{i+1/2,j,k}), \tag{2.82a}$$

$$(\mathbf{D}_y^n)_{i,j+1/2,k} = [\nu + \nu_s]((v_x'')_{i,j+1/2,k} + (v_y'')_{i,j+1/2,k} + (v_z'')_{i,j+1/2,k}), \tag{2.82b}$$

$$(\mathbf{D}_z^n)_{i,j,k+1/2} = [\nu + \nu_s]((w_x'')_{i,j,k+1/2} + (w_y'')_{i,j,k+1/2} + (w_z'')_{i,j,k+1/2}). \tag{2.82c}$$

The second derivative terms in equation (2.82) are approximated by the fourth-order SVV-like polynomial in equation (2.74). We approximate the terms multiplied by α using a second-order central differencing scheme.

$$(u''_x)_{i+1/2,j,k} = a\frac{u_{i+3/2,j,k} - 2u_{i+1/2,j,k} + u_{i-1/2,j,k}}{\Delta x^2} + b\frac{u_{i+5/2,j,k} - 2u_{i+1/2,j,k} + u_{i-3/2,j,k}}{4\Delta x^2}$$
$$- \alpha\frac{u_{i+1,j,k} - 2u_{i-1/2,j,k} + u_{i+1,j,k}}{\Delta x^2} - \alpha\frac{u_{i+5/2,j,k} - 2u_{i+3/2,j,k} + u_{i+1,j,k}}{\Delta x^2}. \tag{2.83}$$

$$(v''_x)_{i,j+1/2,k} = a\frac{v_{i,j+3/2,k} - 2v_{i,j+1/2,k} + v_{i,j-1/2,k}}{\Delta x^2} + b\frac{v_{i,j+5/2,k} - 2v_{i,j+1/2,k} + v_{i,j-3/2,k}}{4\Delta x^2}$$
$$- \alpha\frac{v_{i,j+1,k} - 2v_{i,j-1/2,k} + v_{i,j+1,k}}{\Delta x^2} - \alpha\frac{v_{i,j+5/2,k} - 2v_{i,j+3/2,k} + v_{i,j+1,k}}{\Delta x^2}. \tag{2.84}$$

$$(w''_x)_{i,j,k+1/2} = a\frac{w_{i,j,k+3/2} - 2w_{i,j,k+1/2} + w_{i,j,k-1/2}}{\Delta x^2} + b\frac{w_{i,j,k+5/2} - 2w_{i,j,k+1/2} + w_{i,j,k-3/2}}{4\Delta x^2}$$
$$- \alpha\frac{w_{i,j,k+1} - 2w_{i,j,k-1/2} + w_{i,j,k+1}}{\Delta x^2} - \alpha\frac{w_{i,j,k+5/2} - 2w_{i,j,k+3/2} + w_{i,j,k+1}}{\Delta x^2}. \tag{2.85}$$

The discretized form of other terms in equation (2.82) are given in Appendix C. Substituting these terms in equation (2.82) results in the discretization of the diffusion terms.

Chapter 3

Mathematical Models

3.1 Falling Liquid Films

This section presents the governing equations in the case of the isothermal falling liquid film.

3.1.1 Governing Equations

Consider an isothermal thin liquid film flowing down a plate angled at β, as sketched in figure 3.1. $\beta = 0$ is equivalent to the horizontal direction and $\beta = 90$ is the vertically falling film. The streamwise component of gravity ($g \sin \beta$) drives the flow. The Cartesian coordinate system (x, y, z) is introduced such that x, y, z corresponds to streamwise, cross-stream, and spanwise directions respectively. In such system, the plate is positioned at $y = 0$ and the interface is located at $y = h(x, z, t)$. The following assumptions should be taken into account [13]:

• The liquid is incompressible, meaning that the density remains constant. This assumption holds true for thin films of average thickness less than $1mm$ in which buoyancy can be neglected. Notice that the film thickness cannot be on

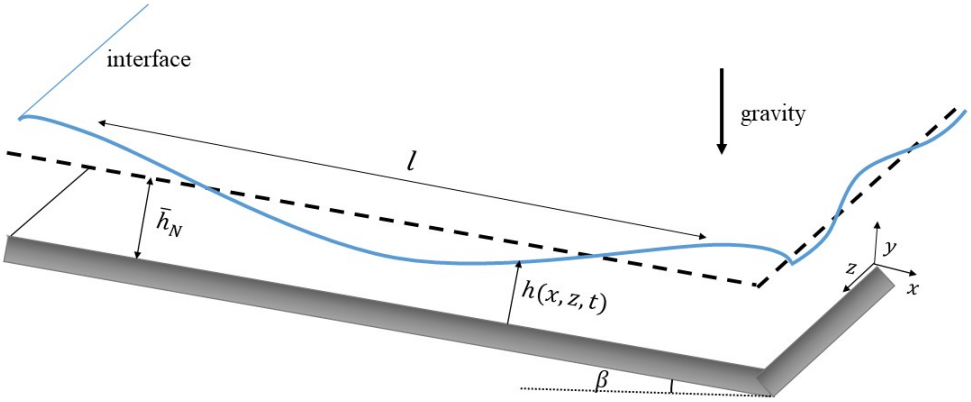

Figure 3.1: A gravity-driven viscous film flowing down an inclined plate. The location of the interface is referred to as $y = h(x, z, t)$. The figure is inspired by [13].

the scale of $100nm$ because intermolecular interactions will be introduced in this range [13].

- The liquid is Newtonian and thus it obeys a linear stress-strain relationship [13].

- The plate is solid, therefore, a no-slip and a no-penetration boundary condition is applicable at the wall.

- The one-fluid approach holds true for this problem in the sense that the viscous stress from the gas is negligible compared to the viscous stress from the liquid which leads to assuming small air to liquid dynamic viscosity ratio (e.g.,$\mu_{air}/\mu_{water} \approx 10^{-2}$). Whereas, the opposite is true for kinematic viscosity (e.g.,$\nu_{air}/\nu_{water} \approx 10$) [13].

- Surface tension σ is constant in the isothermal case.

Considering the assumptions, the continuity and the momentum (Navier-Stokes) equations simplify to:

$$\nabla.\mathbf{v} = 0, \tag{3.1}$$

$$\rho\frac{\partial \mathbf{v}}{\partial t} + \rho\mathbf{A} = -\nabla p + \mathbf{D} + \mathbf{F}, \tag{3.2}$$

where $\mathbf{v}(u, v, w)$ is the velocity vector with components in x,y,z directions respectively. $\mathbf{A} = \nabla.(\mathbf{vv})$ is the advection term and $\mathbf{D} = \nabla.\mu(\nabla\mathbf{v} + \nabla\mathbf{v}^T)$ is the diffusion term (also known as the viscous term). $\mathbf{F} = (g\sin\beta, -g\cos\beta, 0)$ is the contribution of body force with g being the gravitational acceleration.

The following boundary conditions are present:

- At the plate $y = 0$

The no-slip and no-penetration boundary conditions lead to:

$$u = v = w = 0. \tag{3.3}$$

- At the free surface $y = h(x, z, t)$

As a result of isothermal assumption, no evaporation occurs on the interface, therefore, the material derivative of $(y - h)$ remains zero at all points on the interface.

$$\frac{\mathbf{D}}{\mathbf{D}t}(y - h) = 0, \tag{3.4}$$

with $\dfrac{\mathbf{D}}{\mathbf{D}t} = \dfrac{\partial}{\partial t} + \mathbf{v}.\nabla$ being the material derivative. Using this definition, the boundary condition simplifies to:

$$\frac{\mathbf{D}y}{\mathbf{D}t} = \frac{\partial h}{\partial t} + \mathbf{v}.\nabla h. \tag{3.5}$$

The recent relationship means fluid particles of the free surface will remain there at all times and they will be advected with the velocity of the surface [13].

The numerical representation of the free surface will be discussed in 2.1.2.

3.1.2 Base State Solution

The free-surface system described in 3.1.1 has a trivial or base state solution also known as the Nusselt flat film solution [13, 22].

$$u_{liquid}(y) = \frac{\rho_L g \sin\beta}{2\mu_L}(2\bar{h}_N y - y^2) + \frac{\rho_G g \sin\beta}{\mu_L}(Y - \bar{h}_N)y, \tag{3.6}$$

$$u_{gas}(y) = \frac{\rho_G g \sin\beta}{2\mu_G}(2Yy - y^2) + \bar{h}_N^2 g \sin\beta(\frac{\rho_L}{2\mu_L} + \rho_G(\frac{1}{2\mu_G} - \frac{1}{\mu_L})) + Y\bar{h}_N g \sin\beta(\frac{\rho_G}{\mu_L} - \frac{\rho_G}{\mu_G}), \tag{3.7}$$

$$v(y) = w(y) = 0, \tag{3.8}$$

$$P(y) = p_\infty + \rho g \cos\beta(\bar{h}_N - y). \tag{3.9}$$

Equation 3.6 describes the velocity profile in the liquid film ($0 \leq y \leq \bar{h}_N$). Whereas, equation 3.7 characterizes the velocity profile in the gas ($\bar{h}_N \leq y \leq Y$). The two relations culminate in a semi-parabolic velocity profile, which stems from the streamwise component of gravitational acceleration balancing viscous forces. ρ_L, ρ_G, μ_L, and μ_G are the density of the liquid, the density of the gas, the dynamic viscosity of liquid and the dynamic viscosity of the gas respectively. $\bar{h}_N$ corresponds to the height of the flat film. Y is the cross-stream length of the domain. The parameters are indicated in figure 3.2. The Nusselt flat film flow in the isothermal case will develop soon after the inlet to reach the fully developed

flow after which an instability develops [13]. The base state solution will be used as the initial condition for the velocity and pressure solvers in the numerical tool to study the hydrodynamic instability.

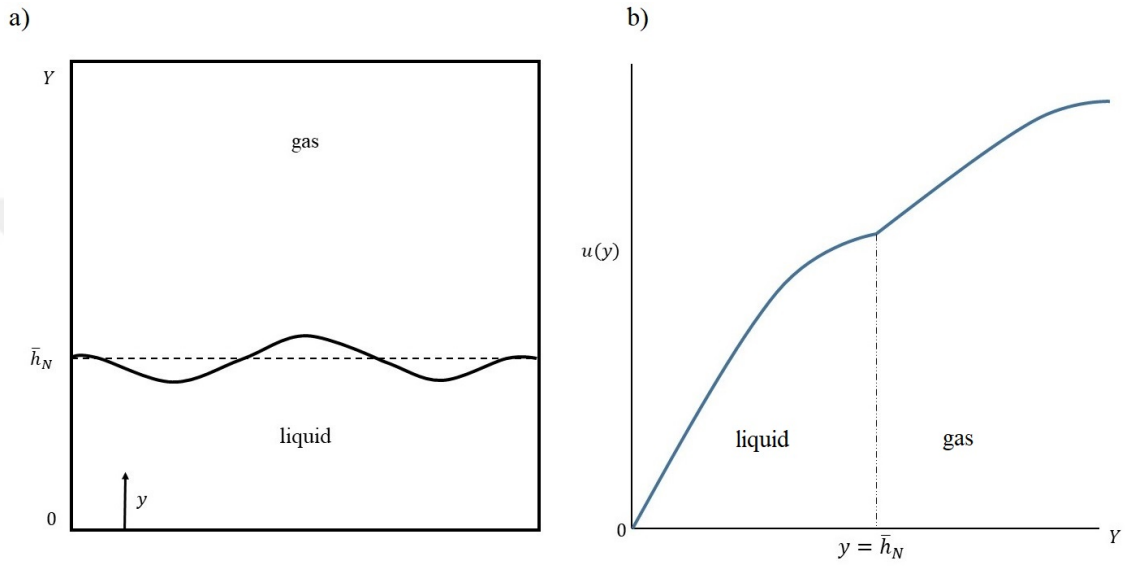

Figure 3.2: a) The schematic of the Nusselt flat film solution. b) The semi-parabolic velocity profiles for liquid and gas at a particular y.

3.1.3 Non-dimensional Equations, Scalings and Parameters

The gravitational acceleration g induces the flow in falling liquid films. Whereas, the kinematic viscosity ν resists the flow. The balance between the two gives rise to the Nusselt flat film solution [13]. A dimensional analysis of the streamwise component of gravity (3.10) and the kinematic viscosity (3.11) forms the base for defining dimensionless parameters and non-dimensional governing equations.

$$g \sin \beta \sim \frac{l_\nu}{t_\nu^2}, \tag{3.10}$$

$$\nu \sim \frac{l_\nu^2}{t_\nu}. \tag{3.11}$$

The dimensionless parameters l_ν and t_ν can be easily obtained from 3.10 and 3.11.

$$l_\nu = (\frac{\nu^2}{g \sin \beta})^{1/3}, \tag{3.12}$$

$$t_\nu = (\frac{\nu}{(g \sin \beta)^2})^{1/3}, \tag{3.13}$$

where l_ν is the viscous gravity length and t_ν is the time scale based on streamwise gravity acceleration and the kinematic viscosity.

Now, we use the Nusselt flat film solution to introduce non-dimensional parameters and equations.

$$(x, y, z)^* \longrightarrow \bar{h}_N(x, y, z), \tag{3.14a}$$

$$h^* \longrightarrow \bar{h}_N h, \tag{3.14b}$$

$$t^* \longrightarrow \frac{t_\nu l_\nu}{\bar{h}_N} t, \tag{3.14c}$$

$$(u, v, w)^* \rightarrow \frac{\bar{h}_N^2}{t_\nu l_\nu}(u, v, w) \tag{3.14d}$$

$$p^* \longrightarrow p_\infty + \rho \frac{l_\nu \bar{h}_N}{t_\nu^2} p. \tag{3.14e}$$

The non-dimensionalization processes in (3.14a) to (3.14e) result in dimensionless parameters and equations.

$$h_N = \frac{\bar{h}_N}{l_\nu}, \tag{3.15}$$

is the dimensionless Nusselt flat film thickness based on viscous gravity length l_ν.

Accordingly, the non-dimensional form of equations (3.1) and (3.2) are:

$$\partial_x u + \partial_y v + \partial_z w = 0, \tag{3.16}$$

$$3Re(\partial_t u + u\partial_x u + v\partial_y u + w\partial_z u) = -\partial_x p + \partial_{xx} u + \partial_{yy} u + \partial_{zz} u + 1, \tag{3.17a}$$

$$3Re(\partial_t v + u\partial_x v + v\partial_y v + w\partial_z v) = -\partial_y p + \partial_{xx} v + \partial_{yy} v + \partial_{zz} v - Ct, \tag{3.17b}$$

$$3Re(\partial_t w + u\partial_x w + v\partial_y w + w\partial_z w) = -\partial_z p + \partial_{xx} w + \partial_{yy} w + \partial_{zz} w. \tag{3.17c}$$

Consequently, the dimensionless form of boundary conditions (3.3) and (3.4) are:

- At the plate $y = 0$:

$$u = v = w = 0. \tag{3.18}$$

- At the free surface $y = h(x, z, t)$:

$$v = \frac{\partial h}{\partial t} + u\frac{\partial h}{\partial x} + w\frac{\partial h}{\partial z}. \tag{3.19}$$

The following dimensionless groups and parameters are important in studying falling liquid films. We will see their application in defining specific case studies in section 4.1.

– The inclination number is the ratio of the cross-stream component of gravitational force to the streamwise component. Its value vanishes for a vertical plate in which hydrostatic pressure is not present. Therefore, it also quantifies the hydrostatic pressure effect in falling films [13]:

$$Ct = \cot\beta. \tag{3.20}$$

– The Kapitza number, named after Leonidovitch Kapitza (1894-1984) is the ratio of surface tension force to the force of inertia independent of the flow rate. The Kapitza number is a function of liquid properties and the plate inclination angle:

$$\Gamma = \frac{\sigma l_\nu}{\rho \nu^2} = \frac{\sigma}{\rho (g \sin \beta)^{1/3} \nu^{4/3}}, \tag{3.21}$$

where σ is the surface tension coefficient. σl_ν is the surface tension force and $\rho\nu^2$ is the inertia force [13].

– The Reynolds number represents a comparison between inertia and viscous forces. Defined as:

$$Re = \frac{\bar{u}_N \bar{h}_N}{\nu} = \frac{\bar{q}_N}{\nu} = \frac{g \sin \beta \bar{h}_N^3}{3\nu^2}, \tag{3.22}$$

where $\bar{u}_N = \dfrac{g \sin \beta \bar{h}_N^3}{3\nu}$ is the average velocity of Nusselt flat film solution and $\bar{h}_N$ is the Nusslet flat film thickness, which is a control parameter of the film thickness in experiments. The specific volumetric flow rate $\bar{q}_N$ is defined as [13]:

$$\bar{q}_N = \int_0^{\bar{h}_N} u(y) dy = \frac{g \sin \beta \bar{h}_N^3}{3\nu}. \tag{3.23}$$

Using (3.15) and (3.12) we can write the dimensionless Nusselt flat film thickness as:

$$h_N = (3Re)^{1/3}. \tag{3.24}$$

– The Weber number is a comparison between the surface tension pressure and the viscous normal stress created by the gravity at the film surface:

$$We = \frac{\sigma}{\rho g \bar{h}_N^2 \sin\beta} = \frac{\Gamma}{h_N^2}. \tag{3.25}$$

In the flows with large We the effect of surface tension pressure is dominant. Whereas, in the flows with small We gravity defines the fluid behavior. Surface deformability due to the flow can be understood from Weber number. Large We corresponds to low deformability since the pressure generated by the viscous forces (responsible for surface deformation) cannot compete with surface tension pressure [13].

– The Froude number is the ratio of inertia gravitational forces [23]:

$$Fr = \frac{\bar{u}_N}{(\bar{h}_N g \sin\beta)^{\frac{1}{2}}} = (\frac{Re}{3})^{\frac{1}{2}}. \tag{3.26}$$

Notice that the Nuseelt film solution is controlled by the flow rate, thus the dimensionless parameters in 3.20 to 3.26 change with the flow rate.

3.1.4 Two-dimensional Waves: Primary Instability

In this section, we introduce the concept of primary instability which is the linear stability of the base state with respect to infinitesimal perturbations. The linear nature of the governing equations allows us to decompose the perturbations into normal modes leading to the Orr-Sommerfeld eigenvalue problem, which is a strong classic theory in the instability analysis of falling liquid films. The instability analysis is not the primary purpose of this document, therefore the theory of primary instability will not be discussed here. For further information on this subject refer to [13] and [9]. However, the Orr-Sommerfeld theory will be used in section 4.1 for the sake of validating the DNS solver.

Chapter 4

Validation and Discussions

4.1 Direct Numerical Simulation (DNS) Solver

In this section, we validate the two-fluid DNS solver, which we developed in section 2.1.1 in the example of hydrodynamic instability of falling liquid films.

4.1.1 Hydrodynamic Instability of Falling Liquid Films

The surface wave instability phenomenon was introduced in section 1.4.1. In this section, we investigate the temporal stability of falling liquid films using our DNS solver elaborated in section 2.1.1. The domain length is settled to $L_x = \frac{2\pi}{k}$ in which $\bar{k}$ is the chosen wavenumber. The domain is represented by a rectangle. The bottom edge corresponds to the inclined surface, at which a no-slip boundary condition is applied. Whereas, an open boundary condition is applied on the top. Periodic boundary conditions are set for the sides. The initial conditions are a combination of the Nusselt film solution as in equations (3.6) and (3.7).

Moreover, an initial disturbance is applied to the interface in the form:

$$h(x) = \bar{h}_N(1 + A\cos(\bar{k}x)), \tag{4.1}$$

where the amplitude of the disturbance, A, is approximated as 1% of the initial film height $\bar{h}_N$. The disturbance is added in order to trigger the instability of the film. For a stable configuration, the disturbance fades away with time and the flow converges to the Nusselt film solution (figure 4.3(a)). On the other hand, for an unstable flow, the disturbance grows linearly at the beginning, followed by the non-linear region, which finally leads to the rupture of the film (figure 4.3(b)).

The DNS tool is verified by comparing the root mean square velocity (U_{rms}) to the growth rate obtained from the linear stability analysis. U_{rms} is calculated at every time step for the liquid phase as follows:

$$U_{rms} = \left[\frac{1}{np}\sum^{np}(u(x,y,z,t) - U(Y))^2\right]^{\frac{1}{2}}, \tag{4.2}$$

where $U(Y)$ is the initial velocity field of Nusselt flat film solution introduced in (3.1.2) and np is the total number of grid points.

A stable case is studied as shown in figure 4.1. Both $Urms$ and $Vrms$ values decline following a fluctuating pattern, which closely agrees with the growth rate predicted by Orr-Sommerfeld linear instability theory. The fluctuations are due to wavenumbers other than the initial mode trying to emerge. However, the overall pattern indicates that the initial disturbance is damped as expected from a stable case. The decrease in disturbance amplitude is clearly observed in figure 4.3(a).

Similarly, hydrodynamic stability analysis is performed on an unstable case. Figure 4.2 shows that the growth rate predicted by Orr-Sommerfeld theory perfectly agrees with the evolution of the instability found by DNS with an error margin within less than 1 percent. Likewise, $Vrms$ values increase with a linear growth rate as predicted by linear instability theory. The unstable nature of the simulation is clearly observed in figure 4.3(b).

All in all, the results follow the growth rate predicted by the Orr-Sommerfeld theory. Thus, we conclude our two-fluid isothermal DNS solver is valid.

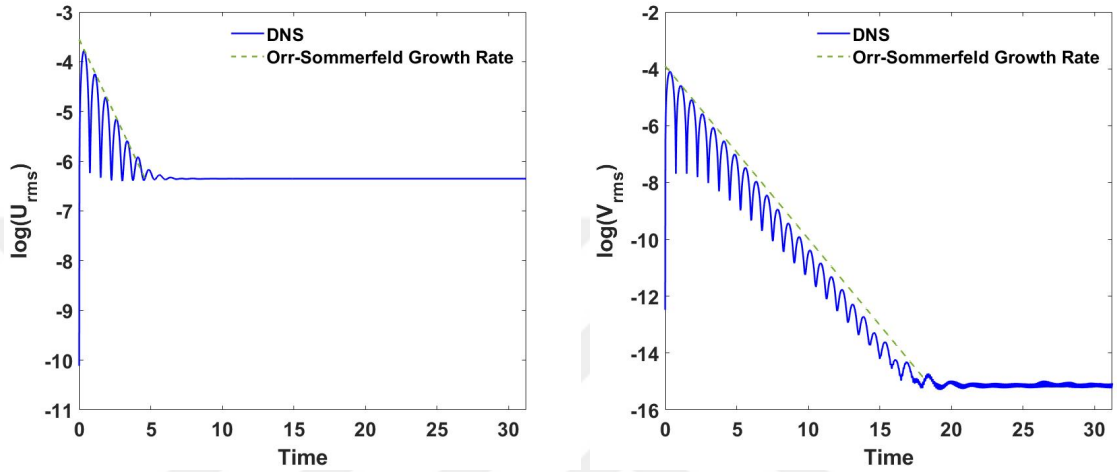

Figure 4.1: The U_{rms} and V_{rms} values in a stable case. We consider an isothermal stable film falling down an inclined surface with $Re = 2$, $Ka = 250$, $\beta = 15°$ and $\bar{k} = 1.2566$. The simulation resolution is 150×100.

We developed a parallel computing code, which uses the MPICH library. The rectangular three-dimensional domain is divided to ns_x, ns_y, and ns_z subdomains in x, y, and z directions respectively. Each subdomain corresponds to a separate process. Whereas, the interface is attributed to a single process. The total number of processes is:

$$n_{processes} = ns_x ns_y ns_z + 1. \tag{4.3}$$

Figure 4.4 indicates that the MPI is successfully implemented as the results from serial and parallel simulations closely match. Furthermore, the presented studies are mesh independent.

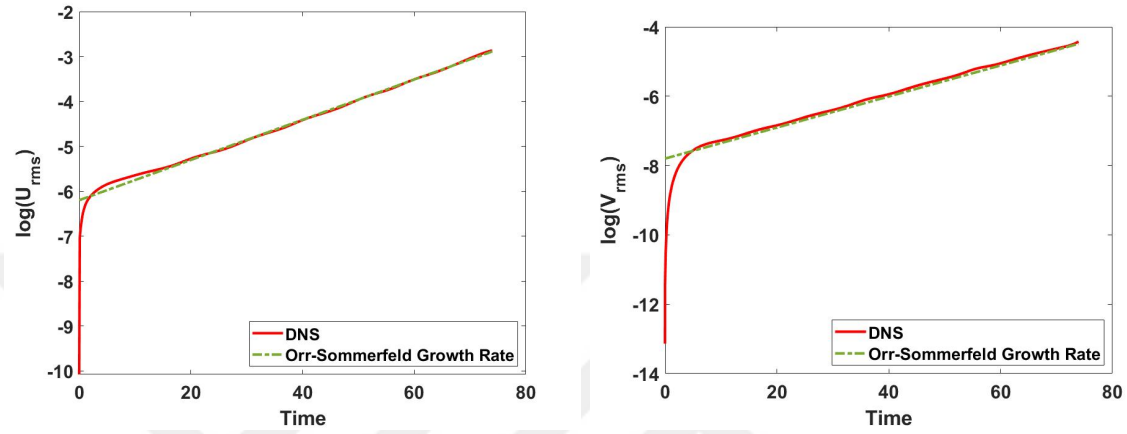

Figure 4.2: The U_{rms} and V_{rms} values in an unstable case. We consider an isothermal unstable film falling down an inclined surface with $Re = 5$, $Ka = 10$, $\beta = 85°$ and $\bar{k} = 0.4488$. The simulation resolution is 150×100.

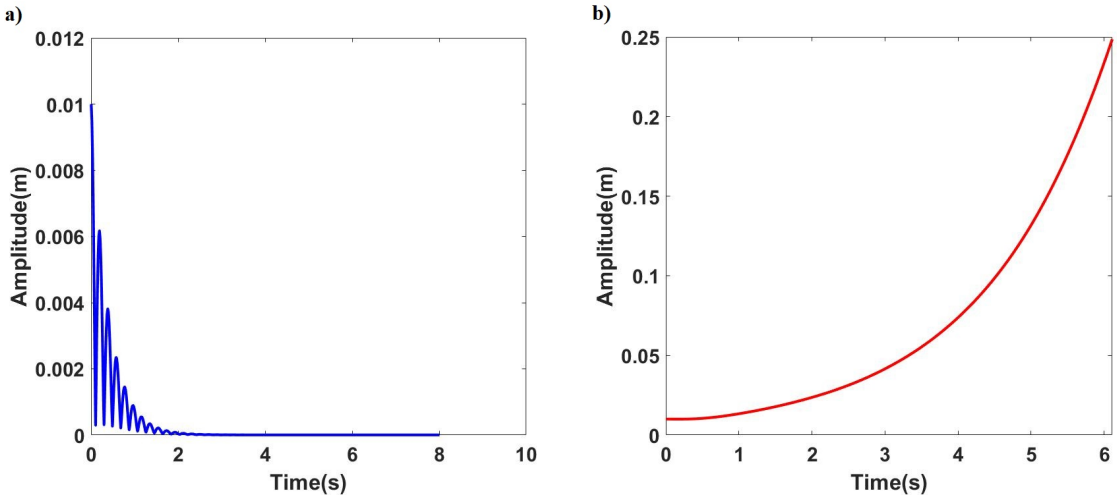

Figure 4.3: The Maximum amplitude in stable and unstable cases. **(a)** Stable case in which disturbance vanishes as the disturbance amplitude reaches zero. **(b)** Unstable case in which disturbances are amplified due to unstable nature of the flow.

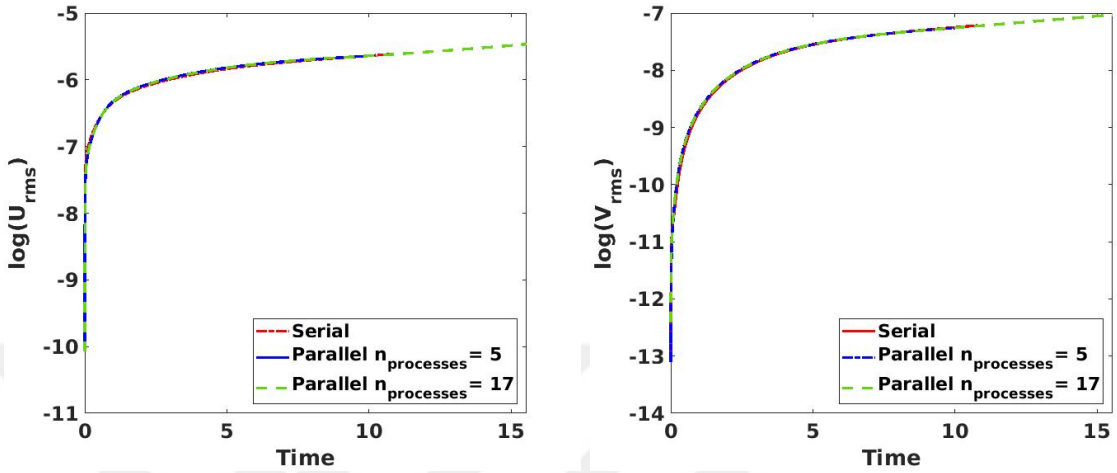

Figure 4.4: A comparison between Parallel and Serial simulations in the unstable case. The growth rate resulting from the Parallel simulations agrees with the serial simulation.

4.2 Large-Eddy Simulation (LES) Solver

In this section, we validate the SVV solver, which we developed in section 2.2.2. first, we investigate the stability of our SVV solver in the benchmark problem of turbulent double layer shear flow. Then, we study the accuracy of the SVV solver using the benchmark problem of turbulent channel flow.

4.2.1 Double Layer Shear Flow

We test the LES Spectral Vanishing Viscosity solver explained in section 2.2.2 in the case study of a turbulent double shear layer flow. The double shear layer includes two longitudinal shear layers that are located at 1/4 and 3/4 of a periodic domain. The transverse perturbation imposed on the flow results in shear-layers rolling up to form two counter-rotating vortices created by the Kelvin-Helmholtz instability mechanism [24,25]. Consider a periodic square domain of length $L = 2$ and a turbulent flow with $\nu = 10^{-4}$, and $Re = 10000$. The initial velocities are

described as:

$$u(y) = \tanh(\epsilon(y - 0.5)), \qquad \text{if } 0 \leq y \leq 1 \tag{4.4a}$$

$$u(y) = \tanh(\epsilon(1.5 - y)), \qquad \text{if } 1 < y \leq 2 \tag{4.4b}$$

$$v(x) = -\delta \cos(\pi x), \tag{4.4c}$$

$$\tag{4.4d}$$

where $\epsilon = 40$ is the thickness of the layer and $\delta = 0.05$ controls the amplitude of the transverse perturbation.

The double layer shear flow is a well-known test case to study the stability of numerical schemes [24]. Any numerically induced disturbances will appear in the form of further spurious vortices that make the simulation reach its stability threshold.

In a similar study, Kirby and Sherwin [26] investigated the double layer shear problem using conventional SVV operators. Figure 4.5 compares the vorticity contour captured at the non-dimensional time $t = 1.87$ to that of Kirby and Sherwin. The SVV solver remains stable and produces a vorticity pattern in agreement with [26].

4.2.2 Channel Flow

We examine the effectiveness of the SVV solver by studying turbulence statistics in the case of a single-phase fully developed turbulent channel flow. Periodic boundary conditions are implemented in the streamwise and spanwise directions. Consider a rectangular domain with $L_x = 5$,$L_y = 2$, and $L_z = 2$ as in [7]. The Reynolds number based on wall shear velocity (u_τ) and channel half width (δ) is given as:

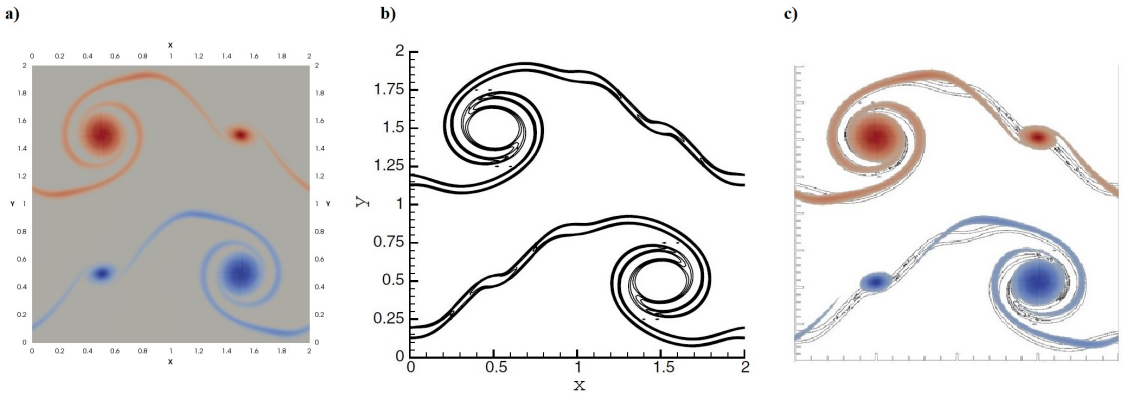

Figure 4.5: A comparison of vorticity contour in double layer shear flow at $t = 1.87$. The simulation resolution is 200×200. a) The solution of SVV solver with $\frac{\nu_0}{\nu} = 10$. b) The solution of Kirby and Sherwin [26] using first-order in time conventional SVV. c) The solution of our SVV solver compared to that of Kirby and Sherwin.

$$Re_\tau = \frac{u_\tau \delta}{\nu} \approx 180. \tag{4.5}$$

The pressure-driven flow is given by [27]:

$$\frac{dp/u_\tau^2}{dx/\delta} = -1. \tag{4.6}$$

Other non-dimensional mean flow variables are:

$$Re_m = \frac{U_m 2\delta}{\nu} \approx 3300, \tag{4.7}$$

$$C_f = \frac{\tau_{wall}}{\frac{1}{2}\rho U_m^2} = 8.18 \times 10^{-3}, \tag{4.8}$$

$$U_m/u\tau = 15.63, \tag{4.9}$$

where U_m is bulk velocity, Re_m is Reynolds number based on bulk velocity and the full channel width, C_f is the skin friction coefficient and τ_{wall} is the wall shear stress [28].

The dimensionless wall distance y^+ is defined as:

$$y^+ = \frac{yu_\tau}{\nu}. \tag{4.10}$$

Figure 4.6 shows the turbulent intensities normalized by the wall shear velocity against the non-dimensional wall distance. The values calculated from the SVV solver closely follow the trend of the turbulent intensities of Karamanos *et al.* [7] obtained from conventional SVV as well as DNS results of Kim *et al.* [28]. The discrepancies between the two methods partly stem from the difference between the resolutions and the element spacings in the cross-stream direction.

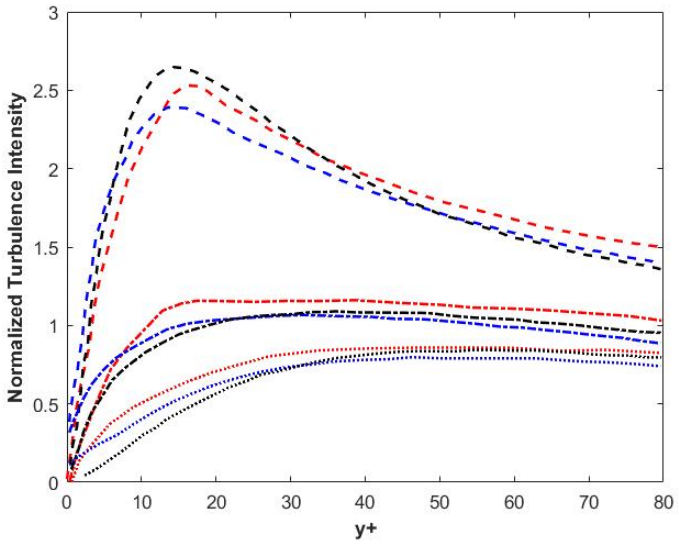

Figure 4.6: A comparison of channel flow turbulence intensities obtained from the SVV solver(red), the conventional SVV of Karamanos *et al.* [7](blue) and the DNS solver of Kim *et al.* [28](black) in the case of single-phase channel flow. $--u_{rms}$, $-.v_rms$, $..w_{rms}$. The simulation resolution is $100 \times 400 \times 100$.

4.3 Hybrid DNS/LES Solver

We combine the two-fluid flow DNS solver and the SVV turbulent flow solver to generate the hybrid DNS/LES solver. We use the solver to simulate the test case of the laminar falling liquid film in presence of turbulent gas.

4.3.1 Turbulent Falling Liquid Films

We investigate the case of the unperturbed laminar falling liquid film in the presence of co-current and counter-current turbulent gas. The no-slip and slip boundary conditions hold at the bottom and top boundaries respectively, while the streamwise direction is periodic. Figure 4.7 shows a sketch of the problem. The turbulent gas is perturbed by imposing a cosine wave, whereas, the liquid film and the interface are initially unperturbed.

The base state solution introduced in section 3.1.2 is implemented as the initial condition in the liquid film. The gas is perturbed by:

$$u_{gas}(y) = u_f y \left(1 - cos(\pi y)\right) rand, \tag{4.11}$$

where u_f is the velocity of film at the interface and $rand$ is a random number between 0 and 1.

Figure 4.8 indicates the liquid film in presence of shearing turbulent gas with an initially flat interface. We observe that the shearing turbulent gas induces perturbations in the liquid film to the point that cosine-like wave patterns form in the liquid. Furthermore, figure 4.10(a) shows that the amplitude of the interface noticeably grows in the presence of turbulent gas.

Similarly, the unperturbed liquid film is affected by the co-flowing turbulent gas as shown in figure 4.9. Growth in the amplitude is observed in figure 4.10(b), however, unlike the case of shearing gas, in this case, the disturbances are smaller

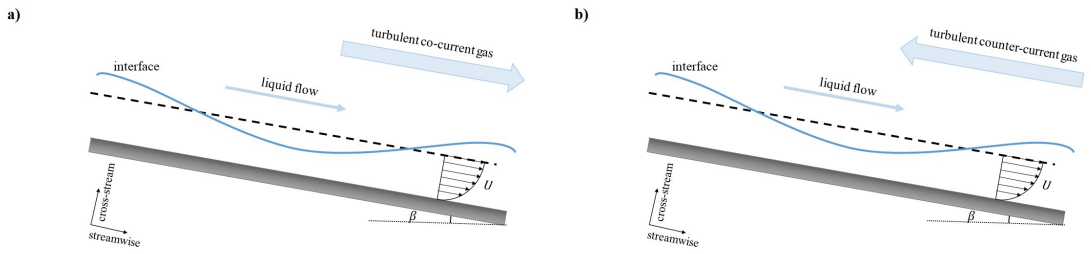

Figure 4.7: Long-wave perturbations form in the presence of turbulent gas. The evolution of interface is the subject of study. Case study: a) falling liquid film in presence of a co-current turbulent gas. b) falling liquid film sheared by a turbulent gas.

in scale and are decaying.

We conclude that our hybrid DNS/LES solver is effective in studying falling liquid films in presence of turbulent gas. A numerical tool that uses the front tracking method to accurately simulate the evolution of the interface in the case study of falling liquid films is unique. Furthermore, using a Spectral Vanishing Viscosity method to model turbulence combined with a front tracking two-fluid solver is a novelty in numerical studies of falling liquid films.

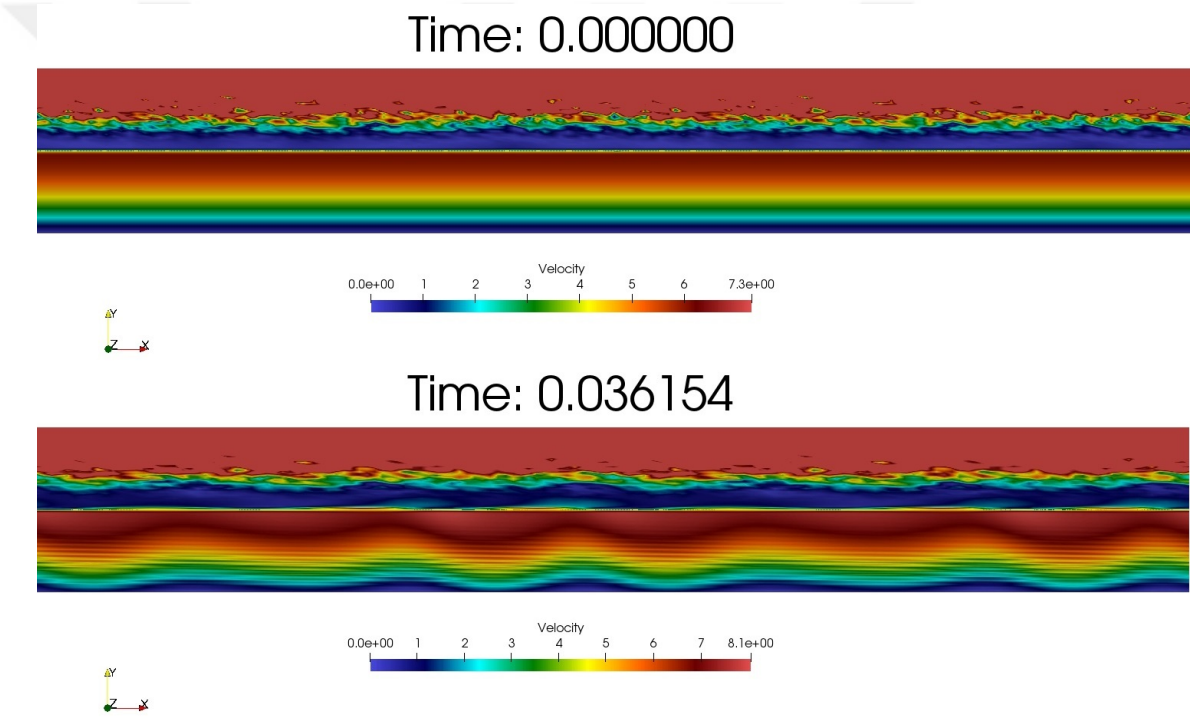

Figure 4.8: Falling liquid film in presence of counter-current turbulent gas. The flow properties are $Re_{liquid} = 2$, $Re_{gas} = 40000$, $Ka = 250$, $\beta = 15°$. The simulation resolution is 150×100. The initially unperturbed interface is affected by the counter-flowing turbulent gas. Cosine-like waves are induced in the film.

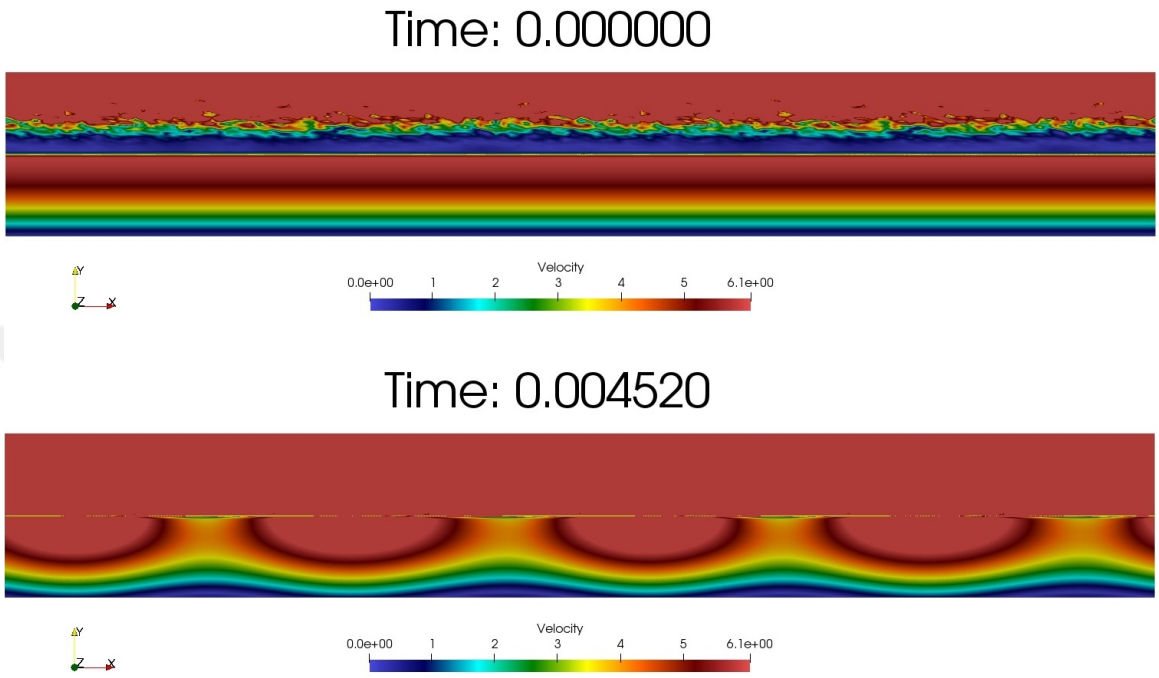

Figure 4.9: Falling liquid film in presence of co-current turbulent gas. The flow properties are $Re_{liquid} = 2$, $Re_{gas} = 40000$, $Ka = 250$, $\beta = 15°$. The simulation resolution is 150×100. The initially unperturbed interface is affected by the co-flowing turbulent gas.

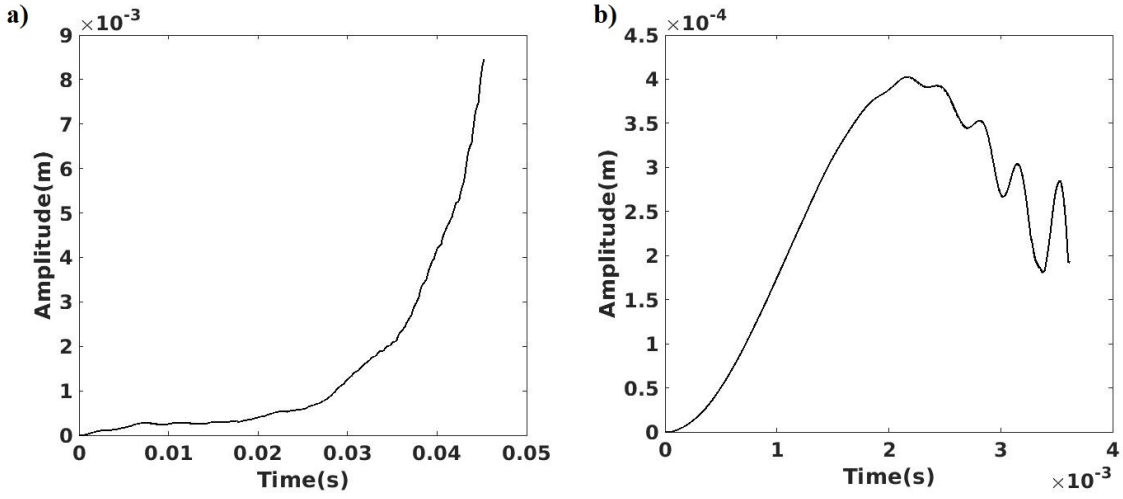

Figure 4.10: a) Time track of the leading hump of the interface in presence of turbulent counter-current gas. b) Time track of the leading hump of the interface in presence of turbulent co-current gas.

Chapter 5

Conclusions and Outlook

5.1 Summary

Numerical modeling of two-fluid flow is a complicated task. In this work, we use the prestigious front tracking method to accurately simulate the evolution of the interface. The two-fluid flow DNS solver is validated against the Orr-Sommerfeld linear instability theory in the case study of hydrodynamic instability of falling liquid films. The DNS solver has excellent agreement with the Orr-Sommerfeld theory in the region of the linear stability for isothermal films. Furthermore, The two-fluid flow DNS tool is useful in understanding the stability of falling liquid films.

DNS of turbulent flow is inefficient in terms of both computational resources and simulation time, especially in simulations of multiphase flow. Therefore, the Large Eddy Simulation (LES) technique is used, which explicitly resolves only the large scales and models the small scales (subgrid scales). Spectral Vanishing Viscosity (SVV) is an LES approach for simulating high Reynolds number turbulent flows. SVV is an alternative LES model, which can control the smallest scales without extra-dissipation at a large scale. An extension of the SVV

method from spectral space to finite-differences is proposed, which uses high-order compact difference formulation to approximate the viscous terms in the Navier-Stokes equations. This scheme is advantageous over conventional SVV due to its straightforward implementation. Furthermore, it does not require up-winding, which makes achieving numerical stability easy in this scheme. In this research, a fourth-order extension of the SVV to finite differences is implemented in the SVV solver. We validated the stability and the accuracy of our SVV solver in the benchmark problems of double layer shear flow and turbulent channel flow respectively.

Finally, we use the hybrid DNS/LES solver to investigate the case study of falling liquid films in presence of turbulent gas. Falling liquid films in presence of turbulence are significantly present in a wide range of engineering applications. However, numerical simulation of falling films is complex due to their multiphase nature. We developed a numerical tool, which accurately simulates the interface evolution using the front-tracking method. The hybrid DNS/LES solver is used to study the case of gravity-driven falling liquid film in presence of co-current and counter-current turbulent gas. The initially unperturbed interface undergoes oscillations as the turbulent gas induces a rise in the interface amplitude.

5.2 Future Work

We showed that the two-fluid DNS solver accurately models gravity-driven isothermal falling liquid film. It is an efficient platform to conduct stability analysis of falling films. The current tool is capable of capturing surface wave instability. However, it can be expanded to account for other phenomena in falling films including the Marangoni effect, evaporation, *etc.*

We used the hybrid DNS/LES solver to study the case of falling liquid films in presence of turbulent gas. However, with slight modifications, the solver can be used to account for other two-fluid systems such as bubbles in turbulent flow field.

The numerical scheme of the hybrid DNS/LES code can be increased in order to incorporate the higher-order extensions of the SVV operator. An optimal and practical scheme is six-order accurate, which requires increasing the accuracy of the spatial discretizations and modifying the number of ghost nodes.

Bibliography

[1] S. K. Lele, "Compact finite difference schemes with spectral-like resolution," *Journal of Computational Physics*, vol. 103, pp. 16–42, Nov. 1992.

[2] G. Tryggvason, R. Scardovelli, and S. Zaleski, *Direct numerical simulations of gas-liquid multiphase flows*. Cambridge University Press, 2011.

[3] S. O. Unverdi and G. Tryggvason, "A front-tracking method for viscous, incompressible, multi-fluid flows," *Journal of Computational Physics*, vol. 100, pp. 25–37, May 1992.

[4] Z. Li, F. A. Jaberi, and T. I.-P. Shih, "A hybrid lagrangian–eulerian particle-level set method for numerical simulations of two-fluid turbulent flows," *International Journal for Numerical Methods in Fluids*, vol. 56, pp. 2271–2300, Apr 2008.

[5] S. B. Pope, *Turbulent Flows*. Cambridge University Press, 2000.

[6] E. Tadmor, "Convergence of spectral methods for nonlinear conservation laws," *SIAM Journal of Numerical Analysis*, vol. 26, pp. 30–44, 1989.

[7] G.-S. Karamanos and G. E. Karniadakis, "A spectral vanishing viscosity method for large-eddy simulations," *Journal of Computational Physics*, vol. 163, no. 1, pp. 22–50, 2000.

[8] E. Lamballais, V. Fortuné, and S. Laizet, "Straightforward high-order numerical dissipation via the viscous term for direct and large eddy simulation," *J. Comput. Phys.*, 2011.

[9] H.-C. Chang and E. A. Demekhin, *Complex wave dynamics on thin films*. No. v. 14 in Studies in interface science, Elsevier, 2002.

[10] P. Colinet, J. C. Legros, and M. G. Velarde, *Nonlinear dynamics of surface-tension-driven instabilities*. 2010.

[11] D. P. Frisk and E. J. Davis, "The enhancement of heat transfer by waves in stratified gas-liquid flow," *International Journal of Heat and Mass Transfer*, vol. 15, pp. 1537–1552, Aug. 1972.

[12] S. L. Goren and R. V. S. Mani, "Mass transfer through horizontal liquid films in wavy motion," *AIChE Journal*, vol. 14, no. 1, pp. 57–61, 1968.

[13] S. Kalliadasis, C. Ruyer-Quil, B. Scheid, and M. G. Velarde, *Falling Liquid Films*, vol. 176 of *Applied Mathematical Sciences*. Springer London, 2012.

[14] L. A. Jurman and M. J. McCready, "Study of waves on thin liquid films sheared by turbulent gas flows," *Physics of Fluids A: Fluid Dynamics*, vol. 1, pp. 522–536, Mar. 1989.

[15] N. Kofman, S. Mergui, and C. Ruyer-Quil, "Characteristics of solitary waves on a falling liquid film sheared by a turbulent counter-current gas flow," *International Journal of Multiphase Flow*, vol. 95, pp. 22–34, Oct. 2017.

[16] S. A. S. K. Sergey Aktershev, Dmitriy Markovich and A. Cherdantsev, "Primary instabilities of liquid film flow sheared by turbulent gas stream," 2009.

[17] S. V. Alekseenko, D. M. Markovich, S. M. Kharlamov, and A. V. Cherdantsev, "Experimental study of the linear stability of a falling liquid film in the presence of a turbulent gas stream," *Fluid Dynamics*, vol. 39, pp. 612–620, Apr. 2004.

[18] M. K. Smith, "The mechanism for the long-wave instability in thin liquid films," *Journal of Fluid Mechanics*, vol. 217, pp. 469–485, Aug. 1990.

[19] T. Dairay, E. Lamballais, S. Laizet, and J. C. Vassilicos, "Numerical dissipation vs. subgrid-scale modelling for large eddy simulation," *Journal of Computational Physics*, vol. 337, pp. 252–274, May 2017.

[20] T. Dairay, V. Fortuné, E. Lamballais, and L. Brizzi, "LES of a turbulent jet impinging on a heated wall using high-order numerical schemes," *International Journal of Heat and Fluid Flow*, vol. 50, pp. 177–187, Dec. 2014.

[21] G. Deskos, S. Laizet, and M. D. Piggott, "Turbulence-resolving simulations of wind turbine wakes," *Renewable Energy*, vol. 134, pp. 989–1002, Apr. 2019.

[22] C. Albert, A. Tezuka, and D. Bothe, "Global linear stability analysis of falling films with inlet and outlet," *Journal of Fluid Mechanics*, vol. 745, pp. 444–486, Apr. 2014.

[23] G. Dietze, W. Rohlfs, K. Nährich, R. Kneer, and B. Scheid, "Three-dimensional flow structures in laminar falling liquid films," *Journal of Fluid Mechanics*, vol. 743, pp. 75–123, Feb. 2014.

[24] C. Coreixas, G. Wissocq, G. Puigt, J.-F. Boussuge, and P. Sagaut, "Recursive regularization step for high-order lattice boltzmann methods," *Physical Review E*, vol. 96, no. 3, p. 033306, 2017.

[25] T. Warburton, L. Pavarino, and J. Hesthaven, "A pseudo-spectral scheme for the incompressible navier–stokes equations using unstructured nodal elements," *Journal of Computational Physics*, vol. 164, pp. 1–21, Dec. 2000.

[26] R. M. Kirby and S. J. Sherwin, "Stabilisation of spectral/hp element methods through spectral vanishing viscosity: Application to fluid mechanics modelling," *Computer Methods in Applied Mechanics and Engineering*, vol. 195, pp. 3128–3144, Apr. 2006.

[27] G.-S. Karamanos, *Large Eddy Simulation using Unstructured Spectral/hp Finite Elements*. Imperial College, Department of Aeronautics, 1999.

[28] J. Kim, P. Moin, and R. Moser, "Turbulence statistics in fully developed channel flow at low reynolds number," *Journal of Fluid Mechanics*, vol. 177, pp. 133–166, Apr 1987.

Appendix A

Discretization of Diffusion Terms

The discretized form of y and z components of the diffusion terms introduced in section 2.1.1 are:

$$(D_y)^n_{i,j+1/2,k} = \mu^n_{i+1/2,j+1/2,k}(\frac{u^n_{i+1/2,j+1,k} - u^n_{i+1/2,j,k}}{\Delta x \Delta y} + \frac{v^n_{i+1,j+1/2,k} - v^n_{i,j+1/2,k}}{\Delta x^2}) -$$
$$\mu^n_{i-1/2,j+1/2,k}(\frac{u^n_{i-1/2,j+1,k} - u^n_{i-1/2,j,k}}{\Delta x \Delta y} + \frac{v^n_{i,j+1/2,k} - v^n_{i,j+1/2,k}}{\Delta x^2}) + 2\mu^n_{i,j+1,k}($$
$$\frac{v^n_{i,j+3/2,k} - v^n_{i,j+1/2,k}}{\Delta y^2}) - 2\mu_{i,j,k}(\frac{v^n_{i,j+1/2,k} - v^n_{i,j-1/2,k}}{\Delta y^2}) + \mu^n_{i,j+1/2,k+1/2}($$
$$\frac{w^n_{i,j+1,k+1/2} - w^n_{i,j,k+1/2}}{\Delta z \Delta y} + \frac{v^n_{i,j+1/2,k+1} - v^n_{i,j+1/2,k}}{\Delta z^2}) - \mu^n_{i,j+1/2,k-1/2}($$
$$\frac{w^n_{i,j+1,k-1/2} - w^n_{i,j,k-1/2}}{\Delta z \Delta y} + \frac{v^n_{i,j+1/2,k} - v^n_{i,j+1/2,k-1}}{\Delta z^2}), \tag{A.1a}$$

$$(D_z)^n_{i,j,k+1/2} = \mu^n_{i+1/2,j,k+1/2}(\frac{u^n_{i+1/2,j,k+1} - u^n_{i+1/2,j,k}}{\Delta x \Delta z} + \frac{w^n_{i+1,j,k+1/2} - w^n_{i,j,k+1/2}}{\Delta x^2}) -$$
$$\mu^n_{i-1/2,j,k+1/2}(\frac{u^n_{i-1/2,j,k+1} - u^n_{i-1/2,j,k}}{\Delta x \Delta z} + \frac{w^n_{i,j,k+1/2} - w^n_{i-1,j,k+1/2}}{\Delta x^2}) + \mu^n_{i,j+1/2,k+1/2}($$
$$\frac{w^n_{i,j+1,k+1,} - w^n_{i,j,k+1/2}}{\Delta y^2} + \frac{v^n_{i,j+1/2,k+1} - v^n_{i,j+1/2,k}}{\Delta y \Delta z}) - \mu^n_{i,j-1/2,k+1/2}($$
$$\frac{w^n_{i,jk+1/2} - w^n_{i,j-1,k+1/2}}{\Delta y^2} + \frac{v^n_{i,j-1/2,k+1} - v^n_{i,j-1/2,k}}{\Delta y \Delta z}) + 2\mu^n_{i,j,k+1}\frac{w^n_{i,j,k+3/2} - w^n_{i,j,k+1/2}}{\Delta z^2} -$$
$$2\mu^n_{i,j,k}\frac{w^n_{i,j,k+1/2} - w^n_{i,j,k-1/2}}{\Delta z^2}. \tag{A.1b}$$

Appendix B

Discretization of Advection Terms

The discretized form of y and z components of the advection terms introduced in section 2.1.1 are:

$$(A_y)^n_{i,j+1/2,k} = \frac{1}{\Delta x}[(\frac{u^n_{i+1/2,j,k} + u^n_{i+1/2,j+1,k}}{2})(\frac{v^n_{i,j+1/2,k} + v^n_{i+1,j+1/2,k}}{2}) - (\frac{u^n_{i-1/2,j,k} + u^n_{i-1/2,j+1,k}}{2})(\frac{v^n_{i,j+1/2,k} + v^n_{i-1,j+1/2,k}}{2})] + \frac{1}{\Delta y}[(\frac{v^n_{i,j+3/2,k} + v^n_{i,j+1/2,k}}{2})^2 - (\frac{v^n_{i,j+1/2,k} + v^n_{i,j-1/2,k}}{2})^2] + \frac{1}{\Delta z}[(\frac{w^n_{i,j,k+1/2} + w^n_{i,j+1,k+1/2}}{2})(\frac{v^n_{i,j+1/2,k} + v^n_{i,j+1/2,k+1}}{2}) - (\frac{w^n_{i,j-1/2,k-1/2} + w^n_{i,j+1/2,k-1/2}}{2})(\frac{v^n_{i,j,k} + v^n_{i,j,k-1}}{2})], \tag{B.1a}$$

$$(A_z)^n_{i,j,k+1/2} = \frac{1}{\Delta x}[(\frac{u^n_{i+1/2,j,k} + u^n_{i+1/2,j,k+1/2}}{2})(\frac{w^n_{i,j,k+1/2} + w^n_{i+1,k,k+1/2}}{2}) - (\frac{u^n_{i-1/2,j,k} + u^n_{i-1/2,j,k+1}}{2})(\frac{w^n_{i,j,k+1/2} + w^n_{i-1,j,k+1/2}}{2})] + \frac{1}{\Delta y}[(\frac{v^n_{i,j+1/2,k} + v^n_{i,j+1/2,k+1}}{2})(\frac{w^n_{i,j,k+1/2} + w^n_{i,j+1,k+1/2}}{2}) - (\frac{v^n_{i,j-1/2,k} + v^n_{i,j-1/2,k+1}}{2})(\frac{w^n_{i,jk+1/2} + w^n_{i,j-1,k+1/2}}{2})] + \frac{1}{\Delta z}[(\frac{w^n_{i,j,k+3/2} + w^n_{i,j,k+1/2}}{2})^2 - (\frac{w^n_{i,j,k-1/2} + w^n_{i,j,k+1/2}}{2})^2]. \tag{B.1b}$$

Appendix C

Discretization of Second Derivative Terms in SVV

The discretized form of y and z components of the second derivative terms introduced in section 2.2.2 are:

$$(u''_y)_{i+1/2,j,k} = a\frac{u_{i+3/2,j,k} - 2u_{i+1/2,j,k} + u_{i-1/2,j,k}}{\Delta y^2} + b\frac{u_{i+5/2,j,k} - 2u_{i+1/2,j,k} + u_{i-3/2,j,k}}{4\Delta y^2} \tag{C.1a}$$
$$- \alpha\frac{u_{i+1,j,k} - 2u_{i-1/2,j,k} + u_{i+1,j,k}}{\Delta y^2} - \alpha\frac{u_{i+5/2,j,k} - 2u_{i+3/2,j,k} + u_{i+1,j,k}}{\Delta y^2},$$

$$(u''_z)_{i+1/2,j,k} = a\frac{u_{i+3/2,j,k} - 2u_{i+1/2,j,k} + u_{i-1/2,j,k}}{\Delta z^2} + b\frac{u_{i+5/2,j,k} - 2u_{i+1/2,j,k} + u_{i-3/2,j,k}}{4\Delta z^2} \tag{C.1b}$$
$$- \alpha\frac{u_{i+1,j,k} - 2u_{i-1/2,j,k} + u_{i+1,j,k}}{\Delta z^2} - \alpha\frac{u_{i+5/2,j,k} - 2u_{i+3/2,j,k} + u_{i+1,j,k}}{\Delta z^2},$$

$$(v''_y)_{i,j+1/2,k} = a\frac{v_{i,j+3/2,k} - 2v_{i,j+1/2,k} + v_{i,j-1/2,k}}{\Delta y^2} + b\frac{v_{i,j+5/2,k} - 2v_{i,j+1/2,k} + v_{i,j-3/2,k}}{4\Delta y^2} \tag{C.2a}$$
$$- \alpha\frac{v_{i,j+1,k} - 2v_{i,j-1/2,k} + v_{i,j+1,k}}{\Delta y^2} - \alpha\frac{v_{i,j+5/2,k} - 2v_{i,j+3/2,k} + v_{i,j+1,k}}{\Delta y^2},$$
$$(v''_z)_{i,j+1/2,k} = a\frac{v_{i,j+3/2,k} - 2v_{i,j+1/2,k} + v_{i,j-1/2,k}}{\Delta z^2} + b\frac{v_{i,j+5/2,k} - 2v_{i,j+1/2,k} + v_{i,j-3/2,k}}{4\Delta z^2} \tag{C.2b}$$
$$- \alpha\frac{v_{i,j+1,k} - 2v_{i,j-1/2,k} + v_{i,j+1,k}}{\Delta z^2} - \alpha\frac{v_{i,j+5/2,k} - 2v_{i,j+3/2,k} + v_{i,j+1,k}}{\Delta z^2},$$

$$(w''_y)_{i,j,k+1/2} = a\frac{w_{i,j,k+3/2} - 2w_{i,j,k+1/2} + w_{i,j,k-1/2}}{\Delta y^2} + b\frac{w_{i,j,k+5/2} - 2w_{i,j,k+1/2} + w_{i,j,k-3/2}}{4\Delta y^2} \tag{C.3a}$$
$$- \alpha\frac{w_{i,j,k+1} - 2w_{i,j,k-1/2} + w_{i,j,k+1}}{\Delta y^2} - \alpha\frac{w_{i,j,k+5/2} - 2w_{i,j,k+3/2} + w_{i,j,k+1}}{\Delta y^2},$$
$$(w''_z)_{i,j,k+1/2} = a\frac{w_{i,j,k+3/2} - 2w_{i,j,k+1/2} + w_{i,j,k-1/2}}{\Delta z^2} + b\frac{w_{i,j,k+5/2} - 2w_{i,j,k+1/2} + w_{i,j,k-3/2}}{4\Delta z^2} \tag{C.3b}$$
$$- \alpha\frac{w_{i,j,k+1} - 2w_{i,j,k-1/2} + w_{i,j,k+1}}{\Delta z^2} - \alpha\frac{w_{i,j,k+5/2} - 2w_{i,j,k+3/2} + w_{i,j,k+1}}{\Delta z^2}.$$